UCLouvain

École polytechnique de Louvain

Characterization of the erosion resistance of coatings for aerospace and windmill applications

Authors : **Rémy Sibille**, **Nathan Tasset**
Supervisor : **Thomas Pardoen**
Readers : **Pierre Bollen**, **Juray De Wilde**
Academic year 2019–2020
Master [120] in Civil Engineering
Master [120] in Electro-mechanical Engineering

Abstract

Water droplet erosion has been an issue for more than 50 years now. Nowadays, the windmill industry is expanding faster than ever and the loss of energy production due to the erosion of the blades is significant.

In the aerospace industry, the damage caused by water droplet erosion on the leading edges reduces their lifetime. Even more today when planes take off regardless of the weather conditions. The environmental considerations push the industry into building planes that will last for a longer period of time, increasing the importance of the erosion resistance of the materials.

This work is divided in two parts : the first one is a state of the art of what is known of the mechanisms responsible for water droplet erosion, the parameters impacting the erosion resistance and all the existing protection solutions, and the second one where erosion tests are performed and the model used for the numerical simulations, its limits and the results are discussed.

Acknowledgements

We would like to thank Professor Thomas Pardoen for guiding us in our reasearches, trusting us in our work and giving us the opportunity to increase our range of skills.

We also wish to thank Pierre Bollen for advising us throughout this work, for taking the time to answer our various questions and providing us guidance through the challenge that *Abaqus* represents.

We wish to extend our thanks to Nathan Klavzer and Frederik Van Loock for their help in material modeling. We are also grateful to Professor Juray De Wilde for taking the time to read our work and be a member of our jury.

Contents

Introduction

In its most popular usage, the word *erosion* is defined as the fact of soil, stone, etc. being gradually damaged and removed by the waves, rain, or wind [1]. In material science however, it is used to describe mechanical damage caused by high speed impingement [2] during solid-solid or solid-liquid interactions. A damage that will appear after a substantial number of cyclic loadings for each type of erosion (particle erosion, liquid erosion, cavitation erosion, slurry erosion, etc.).

Various sectors have shown a clear interest for the studying of water droplet erosion including aerospace and windmill applications. As erosion has a negative impact on the aerodynamic performance of both planes wings and windmills blades, it represents a significant loss. But these two sectors also have another similarity : the use of composite materials for most of their aerodynamic structure.

In the field of aerospace, weight has always been a key factor of the development process. As planes and helicopters must lift their full weight, aluminium was historically used in the design of airplanes for its mechanical properties to weight ratio. In the 70's another solution emerged, offering an even better ratio of mechanical properties to weight : composite materials. The field has since then seen a very fast adoption rate of composite materials to replace aluminium and other metals as they now constitute over 90% of the airframe structure of the Airbus NH90 helicopter and over 50% of of the newest A350 XWB airplane [3]. Unfortunately for some external parts and engine parts, composite materials can not totally replace metals as they do not offer a good resistance to erosion caused by dust or water. This problem becomes more and more dominating as the number of planes taking off and landing every day keeps increasing in an exponential way. To maximise offer and benefits, planes are nowadays sent in the air almost independently of the weather conditions : rain, storm, frost. These conditions can come with water drops, sand, hail that will accelerate the erosion process.

Leading edge erosion also is an important issue for windmill applications such as wind turbines that use light composite materials to reduce the torque on the turbine axis and maximise the transformed energy's quantity. The rough profile caused by the erosion degrades the aerodynamic performance and impacts the structural integrity of the blade [4]. This results in a reduce efficiency and the necessity of operating maintenance and repair.

Different studies [5] [6] [7] [8] estimated the increase of the drag of an eroded blade with a certain diversity (from 50-100% for smaller levels of erosion up to 300-500% for the most severe cases). A better value to help understanding the losses is the Annual Energy Production (AEP) of the turbines. Depending on the study, a severe erosion would cause an AEP reduction between 5% and 25%. For the European offshore wind sector only, Wiser et al. [9] estimated in 2016 a loss of 75 M€/year due to erosion, number increasing every year with the fast growing of the windmill sector.

The costs of maintenance and repair of turbines' blades can not be neglected either given the difficulty to perform them. Furthermore, a repaired blade will need a second intervention between one and two years after the first one (6 months in some cases) [10] and coating applied on a repaired surface will fail nearly 70% quicker [11]. Garrad [12] estimates that an operator of a 500MW offshore wind farm spends between €2.5 million and €9 million per year on turbine maintenance (without taking the losses due to the shutdown into account) while ORE Catapult estimated the combined costs of the repairs and shutdown to €1.5 million per turbine over its lifetime [13].

Part I

State of the art

Chapter 1

Characterization of Water Droplet Erosion Mechanisms

The phenomenon of erosion is very complex, it takes sometimes years before its effects are visible even though the impact of the droplets have an order of magnitude of the millisecond. In this chapter, we will look at the erosion using different scales : the scale of the localised impact and the interface mechanical response, a larger scale where damage mechanisms interact and emphasize each other and we will finally look at the evolution of erosion processes at a larger time scale.

1.1 Liquid-solid impact

To understand the global and complex phenomenon of erosion, we need to focus on the different interactions in the liquid-solid impact caused by one droplet.

When a water droplet hits the solid surface, pressure pulses are generated inside the liquid and close to the liquid/solid interface [14]. Theses pulses are responsible for the formation of a shocked envelop (disturbed region) in the liquid. This envelop lasts for a few microseconds before breaking away, as represented on Fig. 1.1.

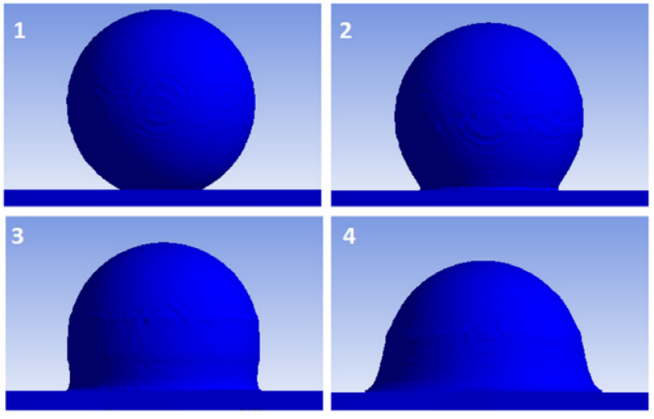

Figure 1.1: Impact development of droplet on a solid surface. Reprinted from [15]

As the liquid is being compressed on the solid, the contact surface increases until it creates a free surface. This is expected to begin when the contact line velocity becomes equal to that of the propagating shock front [14], as illustrated in Fig. 1.2.

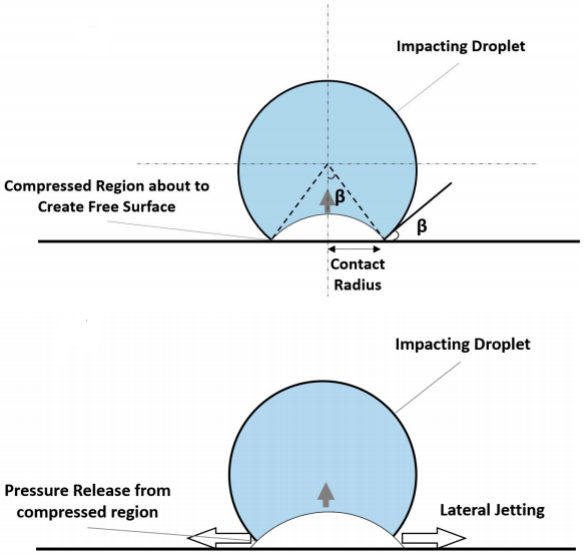

Figure 1.2: Beginning of the lateral jetting formation. Reprinted from [14]

This creates high-velocity flows of liquid in the radial direction. The jet velocity is significantly higher than the impingement velocity, with some measurements suggesting a value up to ten times higher. Both compression stage and radial outflow contribute to water erosion damage.

1.1.1 Compression stage

The phase where the disturbed liquid is applying pressure on the solid is usually referred to as impact or "stagnation" moment. Two important phenomena occur during the impact moment; water hammer pressure and subsequent propagation of stress wave.

Water hammer pressure

Cook [16] was the first to postulate that a constant pressure is induced on a solid surface when it is being impacted by a liquid jet, in 1928. He named it the "water hammer pressure" and proposed this equation to calculate the pressure :

$$P_{w-h} = \rho_0 \, C_0 \, V \ , \tag{1.1}$$

where ρ_0, C_0 and V are the liquid density, the speed of sound in the liquid and the impact speed of the droplet, respectively.

This equation represents a uniform one-dimensional pressure considering a perfectly rigid surface. Dear and Field [17] proposed a modified water hammer equation taking into consideration not only the liquid but also the target body properties, giving this equation

$$P_{w-h} = \frac{\rho_0 \; C_0 \; \rho_s \; C_s \; V}{\rho_0 \; C_0 + \rho_s \; C_s} \; , \tag{1.2}$$

where ρ_s and C_s are the solid density and the speed of sound in the solid, respectively.

This stress is not homogeneous on the whole surface, it has a spatial and temporal distribution that can be provided by numerical analysis. We will focus our interest on the peak stress that occurs at a critical contact radius (r_c), and is quantified, such as Heymann's approximation [18]:

$$P_{peak} = 3 \; \rho_0 \; C_0 \; V \; . \tag{1.3}$$

This pressure will reach its peak value at two different locations in the solid; the first one being the contact edge of the liquid-solid interface and the second one being under the surface of the solid, on the axis of the impacting droplet [19], as represented on Fig.1.3.

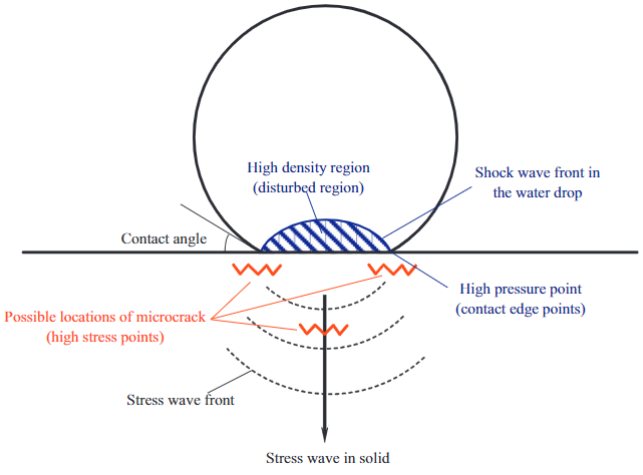

Figure 1.3: Shock wave formation and possible microcrack caused by water drop-solid impact. Reprinted from [19]

Stress waves

"The mechanical equilibrium (state of stress) in the solid is disturbed by the droplet impact and the pressure it creates on the impact zone. The impact will create stress waves in the solid, an initial compressional wave, followed by a shear wave. The interaction

of these waves can be complex and will depend upon impact conditions and material properties. Rayleigh waves moving along the target surface are also generated and the reflected waves can cause tensile waves to appear, as shown in Fig. 1.4. The velocity of these waves also depend on the material properties, mainly its elastic modulus, Poisson's ratio and density. " [14]

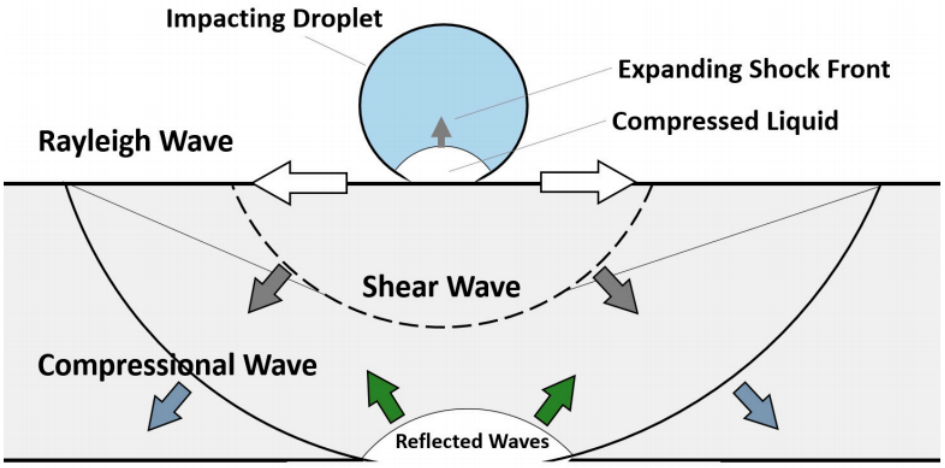

Figure 1.4: Liquid droplet-solid impact interactions. Reprinted from [14]

"The fracture can take place in the solid target due to passage of stress waves having high amplitudes of sufficient duration in excess of the dynamic fracture strength of the target. Stress waves can also interact with microstructural discontinuities resulting in the formation of high tensile stress due to stress concentration. Therefore, stress wave propagation is considered as one of the main mechanisms with which high-speed droplet impact can cause failure" [14].

1.1.2 Flow stage

The lateral outflow happens to depressurize the droplet, to evacuate the energy accumulated in the disturbed region as kinetic energy in the water jets. The jetting is expected to start when the shock front of the compressed liquid region propagating inside droplet creates a free surface. This is expected to begin when the contact line velocity becomes equal to that of the propagating shock front.

Velocity ratio

The velocity of these jets can reach up to several times that of the impact speed. Experiments were performed by Jenkins and Booker [20] to measure the average velocity of lateral jetting of a 2mm diameter droplet at different impact velocity from 100 to 1140m/s :

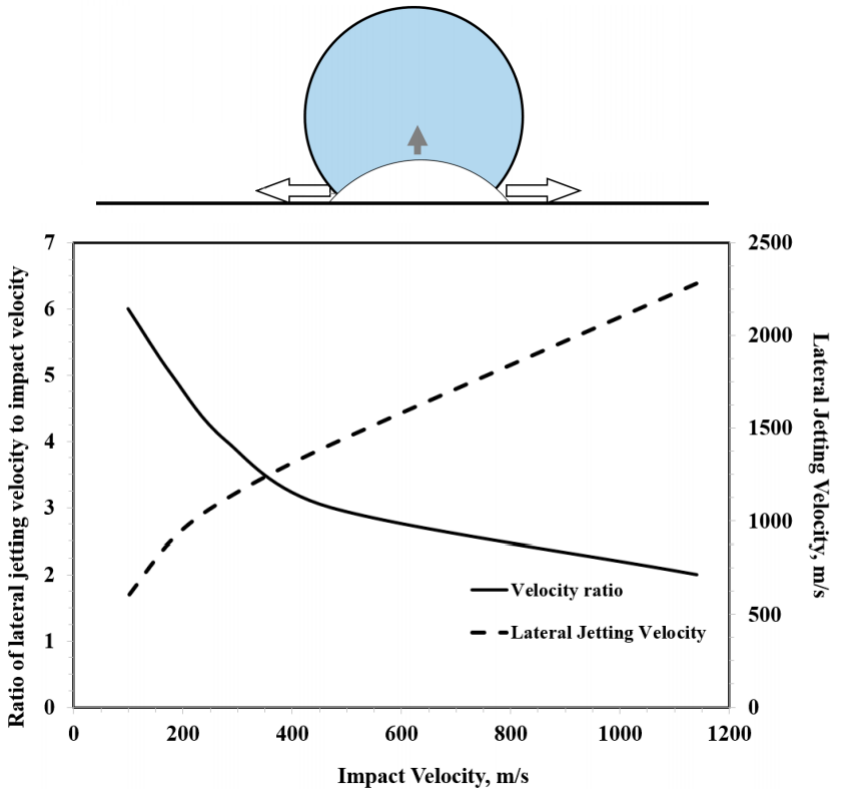

Figure 1.5: Lateral jet velocity as a function of impact velocity. Reprinted from [14]

Fig. 1.5 shows the ratio of lateral jetting velocity to impact velocity and the corresponding lateral jetting velocity based on Jenkins and Booker's [20] experimental results, where the high ratio can be noticed especially at impact speed less than 400 m/s. It can also be noticed that the value of the lateral jetting velocity increases with the increase of the impact velocity. Because of this high velocity, the lateral jetting plays an important role in the initiation of the erosion damage as it can potentially tear surface irregularities.

Lifetime of the jets

Even though the velocity of lateral jets can be very high, the peak velocity only lasts for a small amount of time and decreases exponentially. The time dependence of lateral jetting velocity was clearly demonstrated in the work of Engel [21], where lateral jets of free-falling droplets were observed by a high-speed camera. The emerging lateral jet begins with a very high velocity that decreases with time to eventually reach a value below that of the impact velocity, as shown in Fig. 1.6. The experiment was performed at relatively low impact velocity (less than 10 m/s), and it is still not known if similar behaviour holds at higher impact velocities.

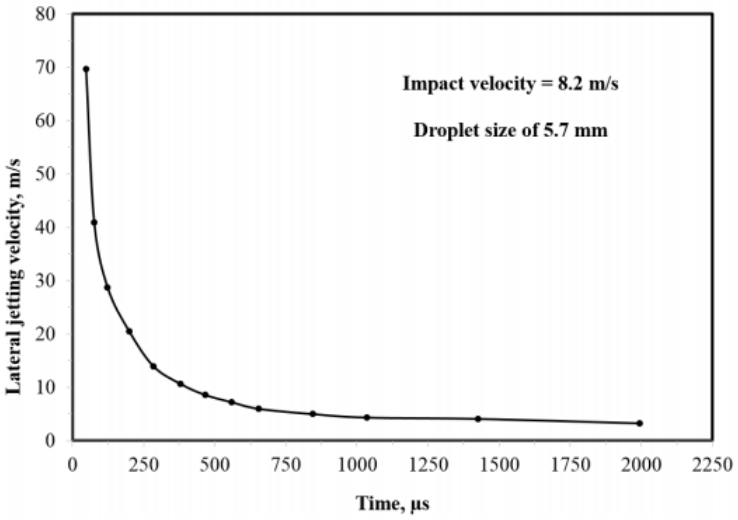

Figure 1.6: Time dependency of lateral jetting velocity. Reprinted from [14]

Engel [21] proposed an equation to estimate the lateral jetting velocity at the beginning of jetting v_l from the impact velocity :

$$v_l = \sqrt{\alpha\ c\ V}\ , \tag{1.4}$$

where c is the speed of sound in the impacting liquid and α is a coefficient that determines the fraction of impact velocity imparted for the liquid molecules. This will be determined by how much of the liquid the compressional wave occupies as it spreads through the spherical drop and creates the free surface for the jetting to emerge.
The value of α approaches the unity as the velocity increases.

1.1.3 Liquid parameters

In the water droplet erosion phenomenon, we have two categories of parameters. The first category includes all the liquid and solid properties like their density, moduli, viscoelasticity behavior, mechanical properties of the target, etc. The second category includes the impingement parameters, we will discuss these parameters in this section.

Impact speed

The impact speed has a significant role on water droplet impact erosion because the induced pressure and kinetic energy of each impact is influenced by the velocity. Coulon [22] described that impact speed is significantly important since it changes the nature of damage (chemical or mechanical). Based on the impact speed, he divided the damage caused by liquid/solid interaction into four groups; corrosion, corrosion-erosion, erosion-corrosion, and erosion. He explained that above a critical impact speed, no chemical

degradation (corrosion) can be seen for liquid/solid interaction and there is only mechanical degradation (erosion). On the other hand, several experimental investigations showed that below a critical impact speed no mechanical degradation occurs.

Experimental data from Heymann [23] revealed that erosion rate is exponentially proportional to the impact speed :

$$ER = a\ (V\ -\ V_c)^n\ , \tag{1.5}$$

where ER is the erosion rate, V the impact velocity, a is a constant, n the speed exponent and V_c is the threshold velocity below which erosion is not likely to take place. The value of the exponent n in water-droplet erosion can reach up to 10. For leading edge erosion applications, Eisenberg et al. [24] reported a speed exponent of $n = 6.7$.

Impact angle

Water erosion is a strong function of normal impact velocity and this velocity varies when changing the impact angle. The influence of impact angle was explored during the incubation period of erosion and before the formation of craters, because the crater formation leads to lose of control of the impact angle. Heymann [23] explained that even during the incubation period studying the influence of impact angle is challenging because of the surface roughness variation. This implies that the impact angle affects only very early stages of erosion and some researchers such as Lee et al. [25] claimed that this effect could be neglected. However, Ahmad [26] recently reported a notable influence of impact angle on water erosion, shown in Fig. 1.7.

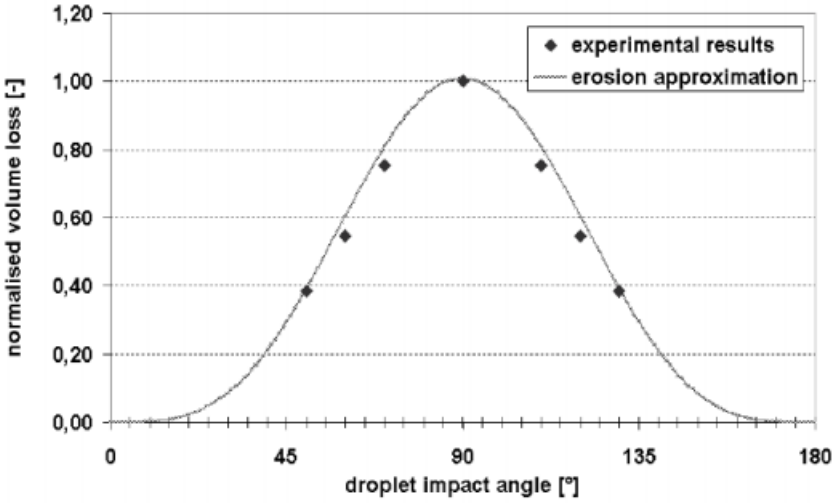

Figure 1.7: Normalized material loss of stainless steel at different impact angles from [26]

The maximum erosion damage, cumulative volume loss after 50h, occurred at impact

angle of 90° which is associated with the maximum normal component of impact velocity.

Droplet size

The droplet size also has a strong influence on the erosion damage, it affects the area exposed to the impacts, time duration of each impact pulse, distribution of impact pressure and the transferred kinetic energy. Larger droplets are likely to cause more erosion than smaller ones for the same total mass of water. This was explained by fatigue-like mechanism of erosion damage and detrimental kinetic energy of water droplets. Hattori and Lin [27] concluded that the volume loss per droplet is proportional to droplet diameter raised to the power 4.7, which indicates the strong influence of the droplet diameter. [14]

Impact speed, impact angle and droplet size are the main impingement parameters that influence the erosion damage. Even though these parameters are not really changeable in our specific case, since we are talking about rain, it is important to know how it interacts in order to create damage on the solid target material.

1.2 Solid damage mechanisms

1.2.1 Direct deformation

This describes the effect of the high water-hammer pressure applied to the surface of the material during the compression stage. The nature of the material is key in determining how this dynamic and transient loading results in damage and subsequent erosion.

Field et al. [28] introduced a model of erosion damage initiation for ductile targets. They proposed that the repetitive impacts of water droplet on a completely smooth surface cause development of damage in four stages, as demonstrated in Fig. 1.8. After initial droplet impacts a shallow depression appears on the surface, shown in Fig. 1.8-a. This depression becomes deeper with further impacts. Once the impacting droplet fills the generated depression, the water is thought to be compressed for a longer period of time. This results in greater impact pressure, Fig. 1.8-b. The next droplet hitting the deformed location experiences different forms of disturbance, shown in Fig. 1.8-c. Here, the angle between the water's free surface and the water/solid interface is important and if it goes beyond a critical angle, the shock envelope breaks away.
The shock waves coming from the walls of deformed area compress the water and make a spear-like central jet. The impact pressure and the strike of this central jet dig the base of depression and generate small central cavity, shown in Fig. 1.8-d. This cavity becomes deeper until the air or water, which can be trapped in the pits, play some cushioning role and suppress further deepening.

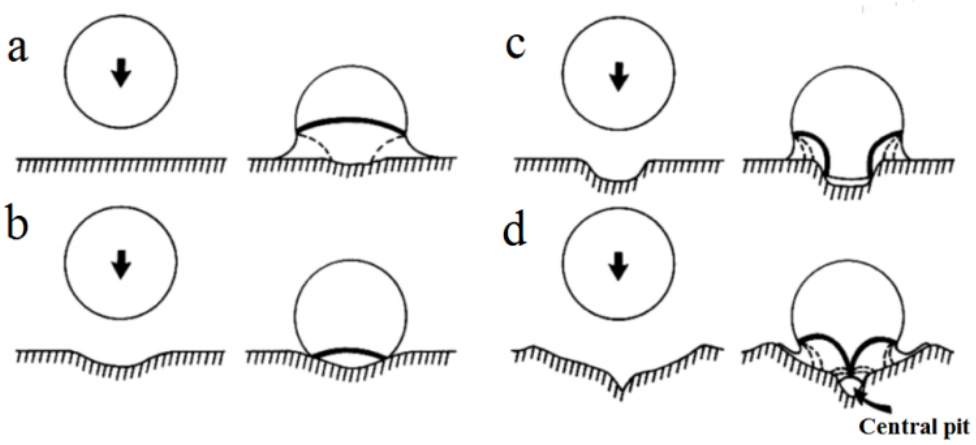

Figure 1.8: Schematic of erosion damage initiation on a ductile solid surface. Reprinted from [29]

1.2.2 Stress wave propagation

The high pressures applied during the compression stage also results in the propagation of stress waves (compression, shear and Rayleigh). These stress waves can interact with features within the material, reinforce, or reach a boundary and reflect, resulting in regions of tensile loading that can lead to damage and erosion.

To understand how the stress waves affect the solid, we use numerical simulation as a powerful modeling tool. Simulations were done by [19] and they made a few basic assumptions :

1. It must describe the spherical water drop in quasi-3-D (or 2-D axisymmetric) space.

2. It must consider the deformation and elasticity of the solid plane. It is important to note that thanks to the short characteristic impact duration (ns) of high-speed impacts on turbine blade, the deformation in the metal is essentially elastic due to strain rate effects and the constraint from materials surrounding the impact site.

3. It must describe the entire period starting from the beginning of impact, until the formation of the lateral jet.

4. It must consider the pressure in the water drop and the stress in the solid simultaneously, and must describe the coupling and difference between them.

Their other assumptions, governing equations and boundary conditions can be found in the paper [30].

To analyse their results, they measured the magnitude of the multi-axial stress field at a material point, called the equivalent stress :

$$\sigma_e = \sqrt{\frac{(\sigma_x - \sigma_r)^2 + (\sigma_r - \sigma_\theta)^2 + (\sigma_\theta - \sigma_x)^2 + 6(\tau_{xr}^2 + \tau_{r\theta}^2 + \tau_{\theta x}^2)}{2}} \,. \tag{1.6}$$

The magnitude of the equivalent stress, non-dimensionalised by the water-hammer pressure, are represented in Fig. 1.9. We see that the pressure wave has spherical form in the disturbed region, increasing away from the origin.

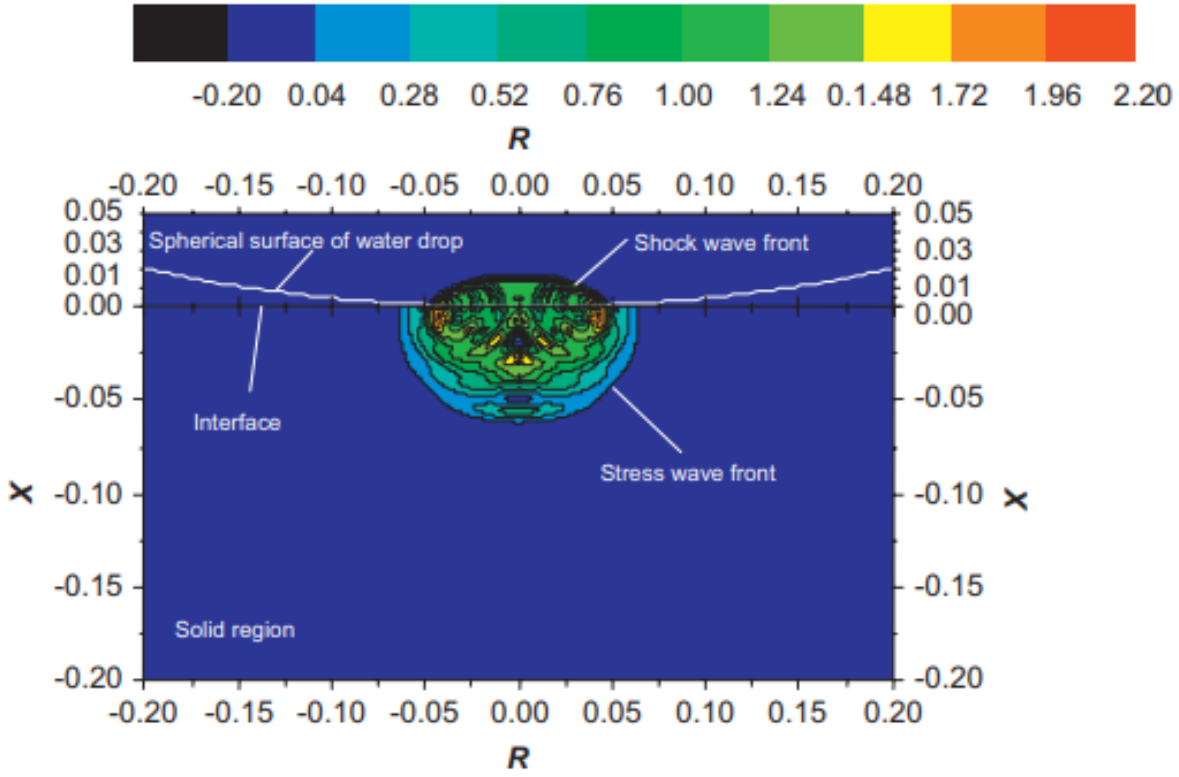

Figure 1.9: Contour plots of pressure distribution and equivalent stress field at t= 5ns. Reprinted from [30]

Two high stress regions appear : near the contact edge where we find the peak pressure mentioned earlier and the other one is near the axis below the surface, caused by the superposition of stress wave crests from axisymetric distribution of sources of disturbance [30].
Considering the water droplet erosion has repetitive and high-frequency impacts, we can explore the damage via fatigue analysis.

For the cyclic loading, the Basquin fatigue relationship is used relating the load amplitude and number of cycles to failure :

$$\sigma_a = \sigma_{f'} \ (2N_f)^b \ , \tag{1.7}$$

where σ_a is the load amplitude, N_f the fatigue lifetime (cycles) and $\sigma_{f'}$ and b material constants [30].
The stress is replaced by equivalent stress and during the loading (impact) and unloading (after the drops breaks into small pieces) the equivalent stress ranges from 0 to $\sigma_{e,max}$.
To adapt the formula for the zero load ratio, Soderberg model suggests that σ_a should be

replaced by $\sigma_a/(1-\sigma_a/\sigma_y)$ (σ_y is the yield strength), and the amplitude is $\sigma_a = \sigma_{e,max}/2$.

$$N_f = \frac{1}{2}\left[\frac{\sigma_{e,max}/\sigma_{f'}}{2(1-(\sigma_{e,max}/2\sigma_{f'})}\right]^{\frac{1}{b}} . \tag{1.8}$$

$\sigma_{e,max}$ can be obtained via an empirical power-law relationship with the impact speed [30]:

$$\sigma_{e,max} = (\rho_0\ c_0\ v_0)\ 9.31(\frac{v_0}{c_0})^{0.39} . \tag{1.9}$$

The fatigue lifetime is explicitly related to the impact speed and material properties. In the simulations conducted in [19] and [30], the number N_f obtained is about 9% lower than the experimental measurement.
We can assume that this little underestimation is caused by the zero load assumption. In reality, there will be stresses in the solid due to residual stresses of previous drops and the possible stress of a protection solution tightened with bolts, for example, that would act as hardening for the solid.

1.2.3 Lateral outflow

The high-velocity lateral jets, produced during the flow stage, can interact with irregularities on the solid surface. The jets hitting the irregularities can produce lateral material flow at the periphery of the impacted area or localized fractures of surface asperities [29].

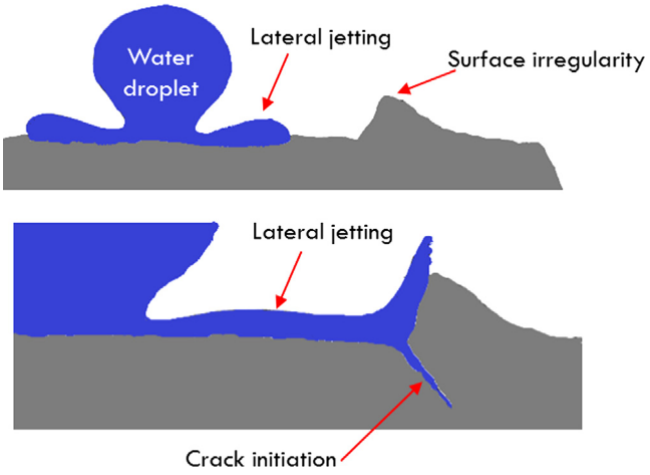

Figure 1.10: Effects of lateral outflow on surface irregularities. Reprinted from [31]

The lateral outflow is also responsible for the cracks initiation, local fracture and micro-void formation.

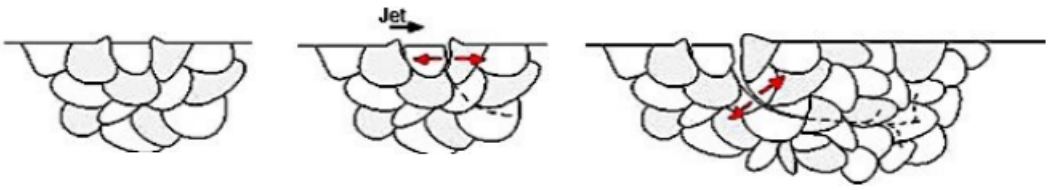

Figure 1.11: Formation of cracks between grains due to lateral outflow. Reprinted from [32]

The high-speed water colliding onto the irregularities will penetrate and separate the grain boundaries as represented in Fig. 1.11 and assist the propagation of the cracks under the surface of the solid.

1.2.4 Hydraulic penetration

"Further droplet impacts on the generated small pits cause a phenomenon called “hydraulic penetration”, which was highlighted as one of the most damaging phenomena in the advanced phases of erosion. Hydraulic penetration was attributed to the formation of spear-like jets inside the cavities. These jets strike the floor of cavities with much larger force compared to the initial droplet impact and bore secondary pits inside the original cavity . Hence, the cavities enlarge and merge together with further impingements. The coalescence of enlarged cavities causes detachment of large fragments and the generation of deep craters. In these stages water hammering, lateral jetting, and water penetration contribute to the erosion damage progress. Droplet impacts on the deep craters result in unhomogeneous stress distribution and formation of different types of pits on the bottom and the sidewall of craters."[29] We can see how this phenomenon acts on the target in Fig. 1.12

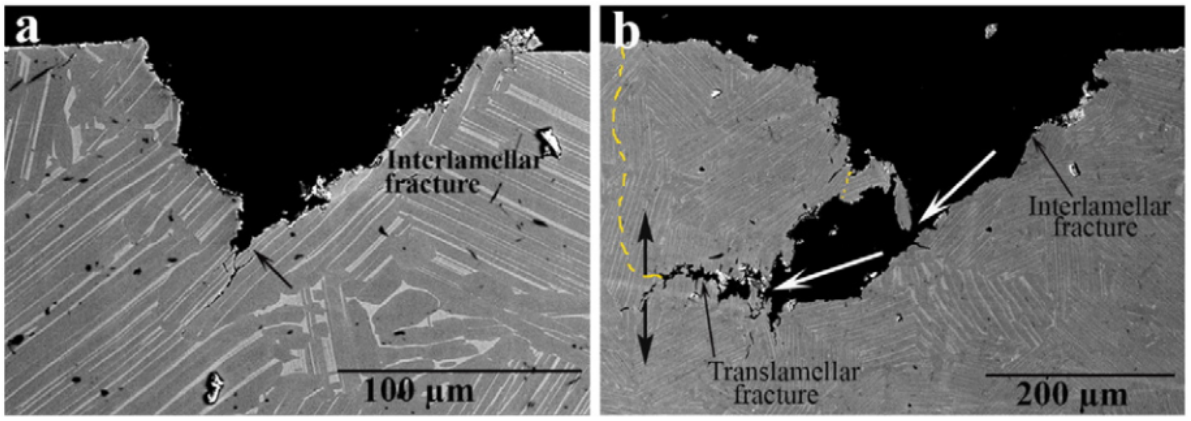

Figure 1.12: Cross-sectional SEM micrographs of isolated erosion craters showing hydraulic penetration at early and evolved stage. Reprinted from [33]

The craters created by the water hammering and the stress waves, called bottom water hammering (BWH) are exposed to hydraulic penetration. The stress is intensified in those craters and new cracks will be created by bottom water penetration (BWP), digging new crack networks under the surface.

The sidewalls of the craters are also attacked by the droplets, mostly through stress wave propagation and hydraulic penetration. The water penetration caused by side jetting occurs mostly at the corners of the erosion crater and leads to the generation of undercutting narrow pits or sub-tunnels [29]. This sidewall water penetration (SWP) is responsible in the widening of the craters.

In Fig. 1.13, these phenomenons are identified using the white arrows. Fig. 1.13-a shows a top view of a typical erosion line for a brittle material.

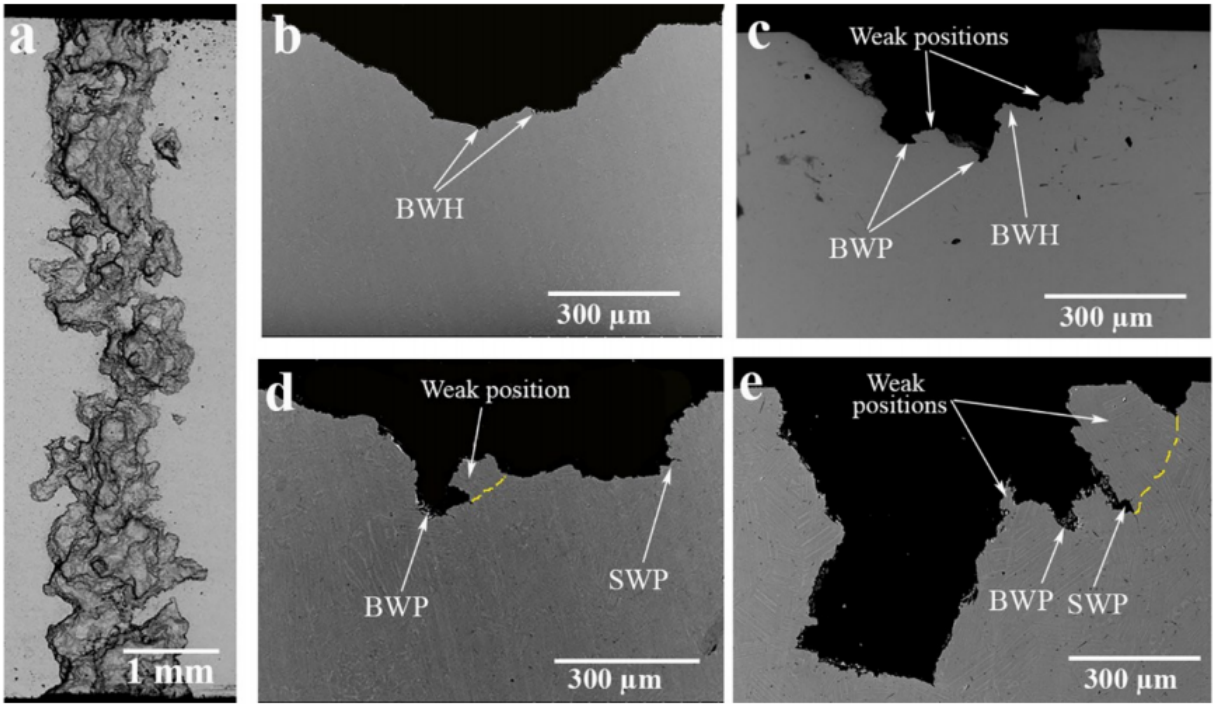

Figure 1.13: (a) SEM micrograph of complete erosion damage line, (b) cross section of eroded TiAl showing wide and shallow pit with relatively smooth surface, (c) cross section of eroded TiAl showing a jagged surface, (d) cross section of eroded TiAl showing formation of an undercutting void at the bottom of crater, (e) cross section of eroded TiAl showing sever damage. Reprinted from [29]

1.3 Time dependence of erosion

All the experiments and observations allowed us to understand that erosion is a time-dependent phenomenon. It shows different erosion rates, each having a different duration. The time dependence of erosion is most of the time represented on a graph showing the material loss as a function of the time (or the number of droplets impacting the solid) as shown in Fig. 1.14.

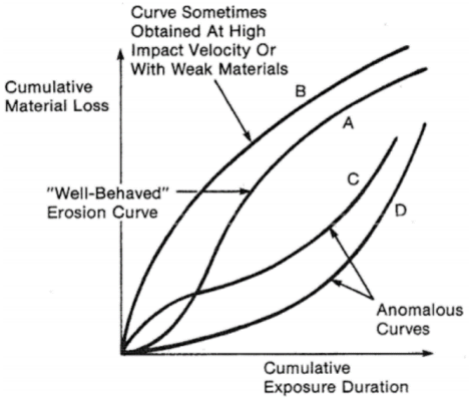

Figure 1.14: Different forms of erosion graphs. Reprinted from [29]

The Curve A is the curve that we should see for most materials showing a good erosion resistance, it has a typical S-shaped form. The Curve B is expected when the erosion conditions (impact speed and droplet size) are especially rough for the target. Curves C and D are anomalous curve forms and cannot be accepted. Heymann [18] separates the typical curve in 5 different stages.

Incubation stage

The first stage is called the incubation. In this period, droplets will start increasing the roughness and create little material flow of the solid surface due to repetitive impacts but this will cause no material loss, resulting in an almost flat curve for this stage. Micro-cracking can also happen in this early stage.

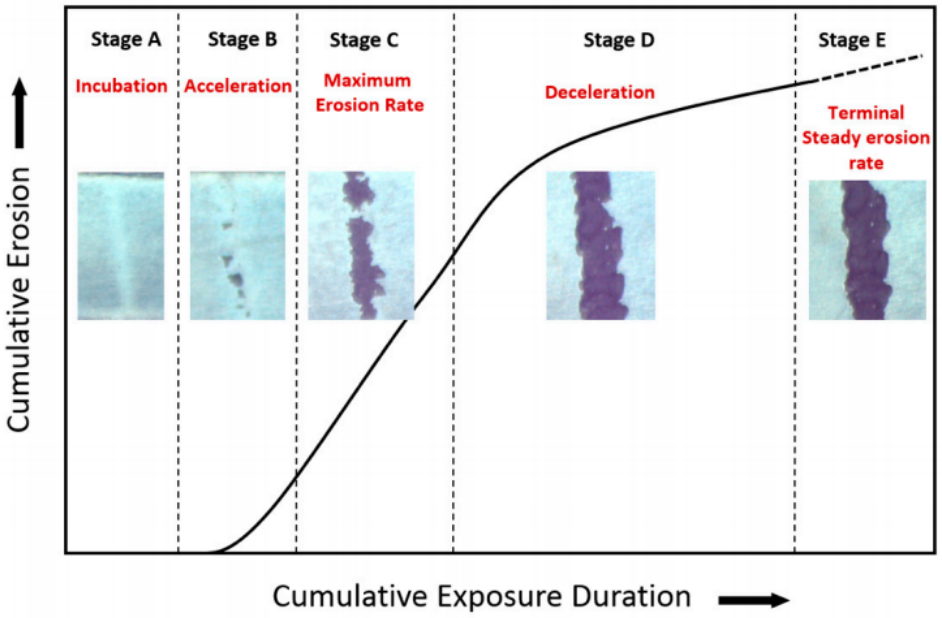

Figure 1.15: Typical stages in water droplet erosion damage curves. Reprinted from [14]

There is almost no damage visible to the unaided eye, except for the change from a mirror-like to a non-reflective surface over the impacted area. This stage is short and sometimes not even exists if the impact conditions are severe, resulting in a B-type curve as depicted in Fig. 1.14.

Acceleration stage

In the acceleration stage, the material loss starts to increase. The little pits and cracks start merging together, resulting in the formation of bigger craters. During this stage the erosion rate increases quickly until it reaches its maximum value.

Maximum erosion rate stage

In this stage, the erosion rate remains constant at its peak value. The cracks keep propagating due to local stress concentration, the craters continue to merge and become deeper and larger.

Deceleration stage

Once the craters attain certain depth, the erosion rate starts to decrease from 25 to 50 % compared to the maximum erosion rate value, this decline is easily visible on Fig. 1.16-b

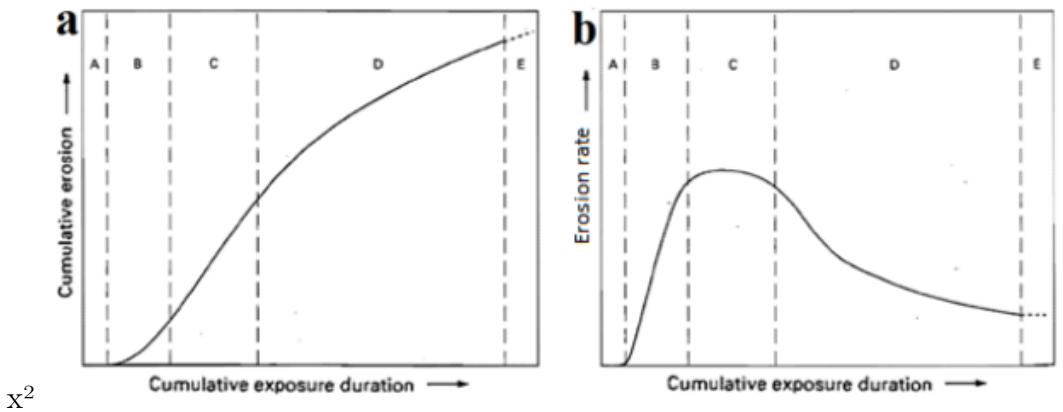

Figure 1.16: (a) Typical water droplet erosion and (b) erosion rate graphs showing five different stages. Reprinted from [29]

The high roughness of the pits and the peaks will change the stress distribution of the impacting droplets and reduce the damage. Furthermore, since the craters are deeper, water can be trapped at the bottom and plays a shock absorber role for the solid, also reducing the erosion damage.

Terminal steady state stage

Once all the craters have merged, a complete erosion line appears on the solid surface. The erosion rate will decelerate until it reaches a constant value in the terminal stage. Although the previous stages occur in a similar way for all erosion tests, the terminal stage does not follow the rule. The erosion rate either continues to decline or shows a series of fluctuations. In some brittle materials and coatings, the erosion rate after the deceleration period starts to rapidly increase in what is called the catastrophic stage [14].

Chapter 2

Effective Parameters for Water Droplet Erosion Damage

The different erosion mechanisms being known, it is interesting to wonder what are the parameters and mechanical properties of the target that play a role in the erosion strength of a material.

A quantitative study is lead in the second part of this thesis where tests were conducted for different materials using coatings. In this section,we will only discuss a few parameters often mentioned in the literature that are not studied in the second part.

2.1 Target material properties

2.1.1 Hardness

The non-dimensional erosion rate V_m is often used in the world of erosion and is defined as the erosion volume in a unit time over local volume flux of liquid. This erosion rate is assumed to be proportional to V^n where V is the droplet velocity and n is the power index ranging for 2 to 7 (often 5 for water droplet erosion). This large range is due to the difference in the experimental conditions [34].

The water droplet erosion is highly influenced by the material hardness, defined as the resistance to a localized plastic deformation induced by a mechanical indentation. A common measure for hardness is H_v, called Vickers hardness and obtained following a precise procedure [35] .

Japanese researchers [34] tried to determine quantitatively the relation between the erosion rate and the hardness by performing erosion tests using a spray jet on different materials with a wide range of hardness.
Previous studies reported that the erosion rate increases proportionally to the Vickers hardness of the material to the power -3.45 in the droplet velocity below 100 m/s and to the power -2.75 above 150 m/s [36].

After measuring the erosion damage on different aluminiums and steels, the non-dimensional erosion rate can be expressed by this equation :

$$V_m = c_2 \left(\frac{H_v}{H_{vAl}}\right)^{-4.5} V^7 \left(1 + c_3 \left(\frac{h}{d}\right)\right)^{c_4}, \tag{2.1}$$

where H_v and H_{vAl} are respectively the specimen and aluminium Vickers hardness, V the droplet velocity, h the liquid film thickness, d the droplet diameter and c_2, c_3, c_4 empirical constants. The experiment demonstrates that the erosion rate decreases with increasing hardness and the liquid film thickness [34].

2.1.2 Impedance

The impedance Z of a material, which is the product of the density ρ and the wave propagation velocity c, influences the magnitude and the velocity of shock waves that are generated in materials. Australian researchers [37] investigated on the shock wave propagation through impedance-graded multi-metallic (IGMM) systems and how the variation of impedance can cause higher/lower stresses in the material and delamination at the interface.

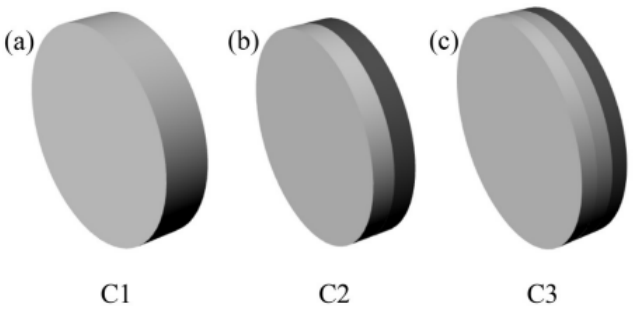

Figure 2.1: (a) Monolithic, (b) bi-metallic and (c) tri-metallic material combination samples used in [37]

High strength steel, aluminium and titanium were used for their tests to resist to a high velocity (up to 1000 m/s) flyer impact. They used a gas gun on the samples to obtain experimental data and then modeled the problem using the finite element code LS-DYNA to understand the time dependant mechanical response of the materials. Their results for a steel-titanium test is represented on Fig. 2.2.

They observed the results for different metal combinations and drew some conclusions for their problem that can also be also be applied for our water droplet erosion phenomenon :

- Hugoniot Elastic Limit (HEL) is an important magnitude to determine the nature

of stress waves, if the initial stress wave exceeds the HEL of the first material, shock waves will propagate in the target

$$HEL = \frac{1-\nu}{1-2\nu} Y_d \,, \tag{2.2}$$

where ν is the Poisson's ration and Y_d the dynamic yield stress of the target material.

- While maintaining a constant total thickness, introducing a material with lower impedance at the back for the target reduces significantly the stress transmitted at the back of the target, and this reduction happens even the though the material introduced is weaker, in terms of yield stress.

- The rise time is defined as the time interval between the magnitude of the shock wave corresponding to the HEL and the initial peak value, a low rise time means a quick rise of the magnitude and thus a strong shock wave.

  Adding a material with less impedance behind the target increases the rise time and less damage will be observed at the back of the sample.

- Impedance mismatch at the interface will emphasize the tensile stresses created by the reflected waves. Since these tensile stresses have an important role in the damage mechanisms, it is suggested to use gradual reductions of the impedance, in order to protect the target from this damage.

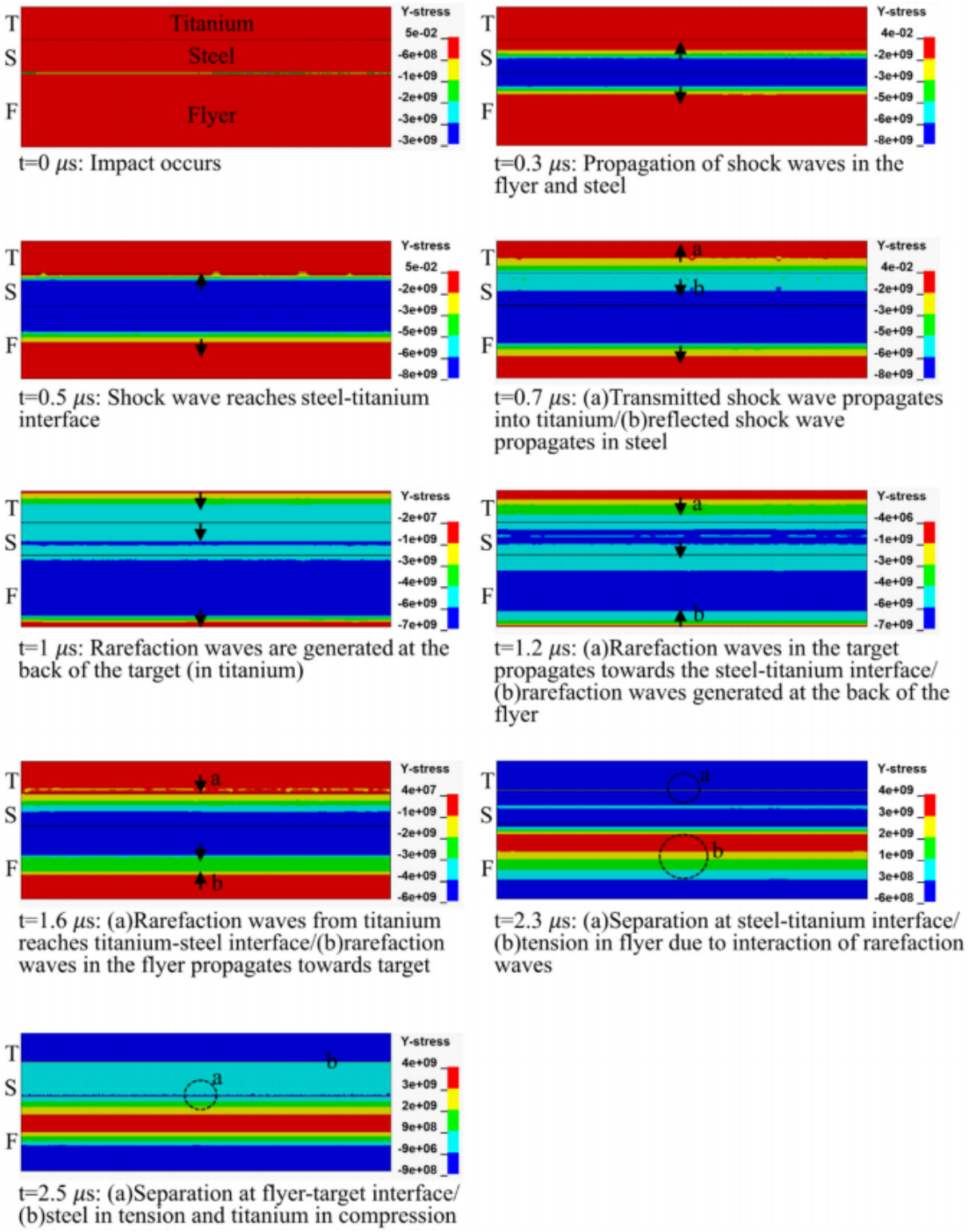

Figure 2.2: Sequential captures from the numerical simulations, representing the stress waves propagation. Reprinted from [37]

2.2 Initial roughness

Most water droplet erosion suffers from the influence of surface roughness during the erosion process. The surface's irregularities increase with the number of droplet impacts on the surface. The droplet impact forces initiate surface cracks and propagate crack growth along the grain boundary of the material [27]. Previous studies have indicated that rough surface erosion is accelerated in the incubation stage. However, the erosion mechanism on rough surfaces remains unclear, because the erosion depends on both the surface roughness geometry, and the liquid-film on the surface during actual erosion conditions. The influence of liquid–film on WDE is a key parameter in understanding the effect of surface roughness. [38]

Fujisawa et al. investigated WDE on W and V groove surfaces (V groove is caused by removal of the groove peak) both experimentally and numerically. They resumed their results with the three following points:

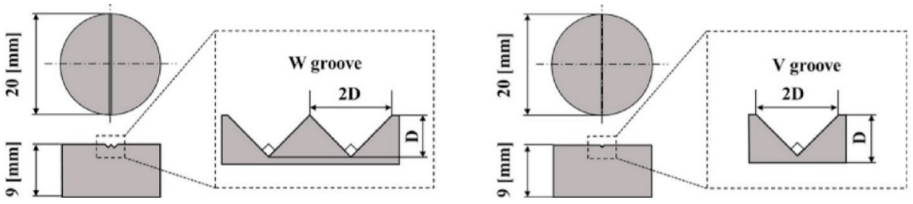

Figure 2.3: Test specimens (W & V grooves) [38]

- Tests on aluminium on W and V grooves for various groove depths ranging from 15 to 100 μm showed an higher erosion rate on the W groove than on the V groove, due to the removal of groove peak on the W groove in the early erosion. This resulted in the high erosion rate for the W groove, which increased with an increase in the groove depth.

- The peak of the W groove was highly deformed by WDE, resulting in the removal of the groove peak. Cross–sectional observations indicated that the groove peak removal for the W groove was caused by the erosion initiation on the groove trough. But also the erosion intrusion under the groove peak.

- The highest impact pressure was generated on the groove peak and trough during erosion when simulating the liquid droplet impingement on the W groove with liquid film. High pressure on the groove peak occurs when the droplet impact is located right above the peak. While the high pressure impacts were caused on the groove trough by droplets impacting above the groove trough or the middle impact (between peak and trough). As a result, WDE will be more often observed on the groove trough.

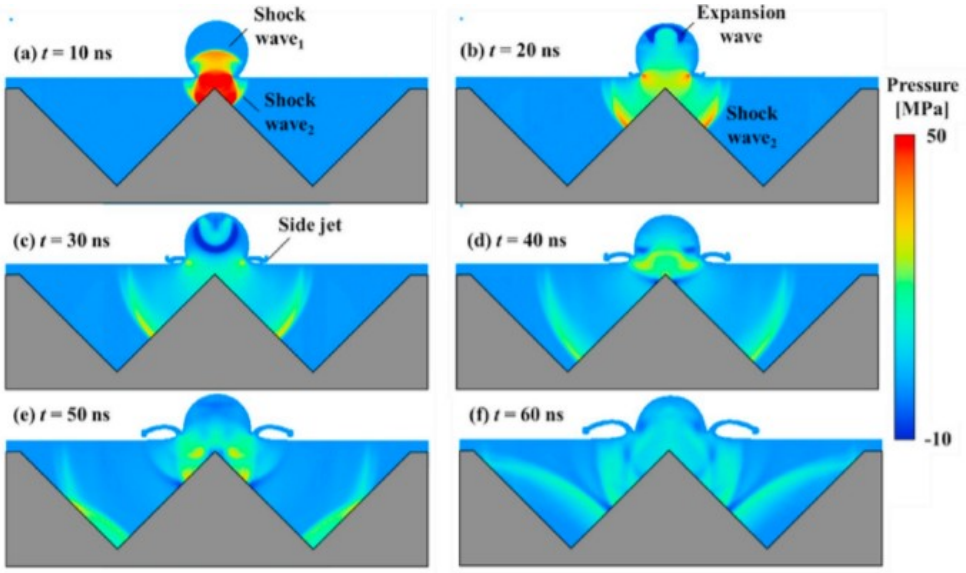

Figure 2.4: Pressure contours and time variation of surface pressures by groove peak impact. Reprinted from [38]

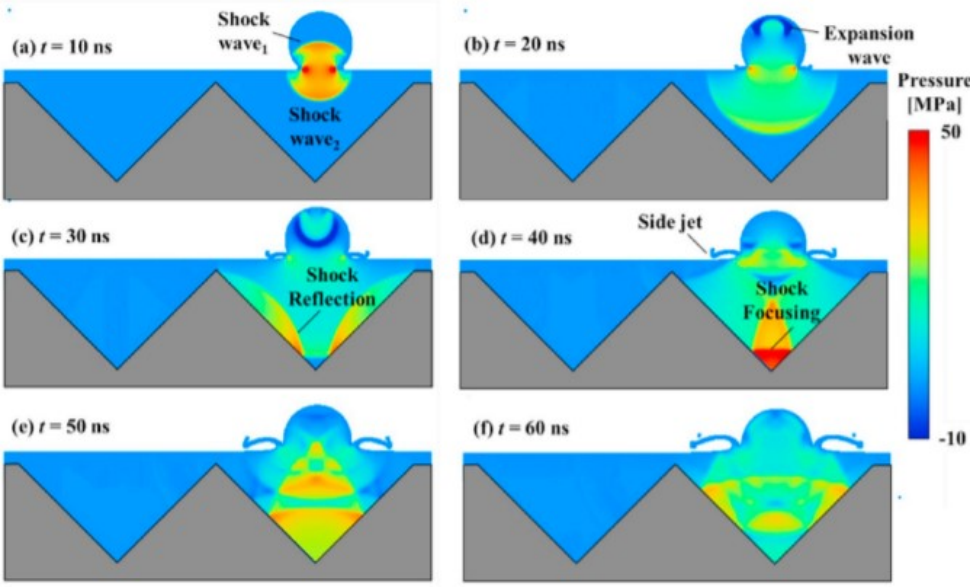

Figure 2.5: Pressure contours and time variation of surface pressures at groove trough impact. Reprinted from [38]

Chapter 3

Protection Solutions

On this date, various protection solutions exist to increase the lifetime of composite leading edges. With the increasing usage of planes and wind turbines, selecting the right leading edge protection is more important than ever and the quality of these solutions follows the same path as more and more people work on the problematic. In this chapter, a description of these various protection systems are presented. The redaction of this chapter was based on the readings of mainly two documents *"Wind Turbine Blade Leading Edge Erosion: An investigation of rain droplet and hailstone impact induced damage mechanisms"* from M. Keegan [39] and *"The increasing importance of leading edge erosion and a review of existing protection solutions"* from R. Herring, K. Dyer, F. Martin and C. Ward [4].

3.1 Coatings

Made of impact resistant materials, coatings are a protection solution that are directly applied to the leading edge's surface. They can be applied with two different techniques, either in-mould or post-mould.

The in-mould solution consists of applying during the manufacturing process a thermosetting polymer layer, gelcoat, to the leading edge directly in the mould (Fig.3.1). The fibers are laid on the gelcoat after this protection layer, typically polyepoxide, polyester or polyurethane, is set at the bottom of the mould. This way, the gelcoat will become the external protection layer after the blade/wing is removed from the mould. A resin is the added to infuse the fibers. The curing of the assembly will then form a chemical bond between the composite material and the gelcoat. An additional manufacturing step is saved using the in-mould solution but a sufficient adhesion between the composite laminate and the gelcoat is required in order to meet the needed short and long term mechanical performances.

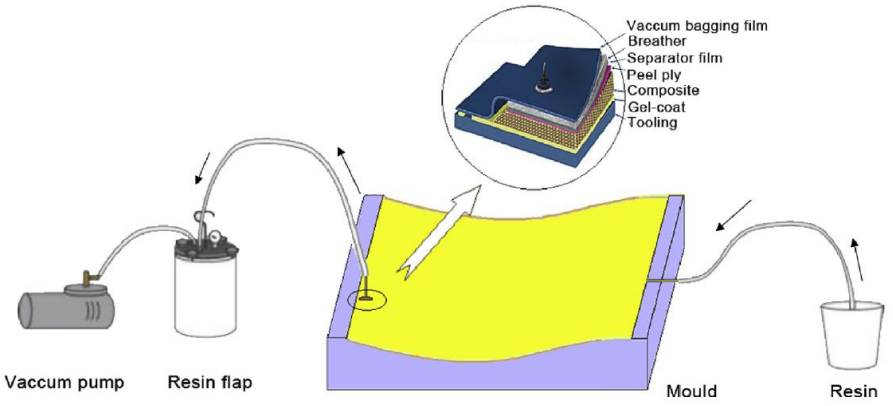

Figure 3.1: In-mould technique for coating application. Reprinted from [40].

The post-mould solution on the other side consists of applying after the manufacturing process, flexible coatings to the surface of the leading edge. Flexible materials such as high erosion resistant elastomers (mainly polyurethane) can be used with this technique. There are different applying techniques such as rollers, spraying, different chemical and physical deposition, etc. (a few examples are represented on Fig. 3.2). First the surface is covered with several filler layers to reduce the roughness of the surface. The flexible coating is then applied on the smooth surface. A primer layer is sometimes added between the filler and the coating to increase the adhesion of the coating [41]. The coating itself can be constituted of a various number of layers. As much as it may provide a better damping to water droplet erosion, it could also accelerate the erosion due to the delamination between layers as the number of interfaces increases.

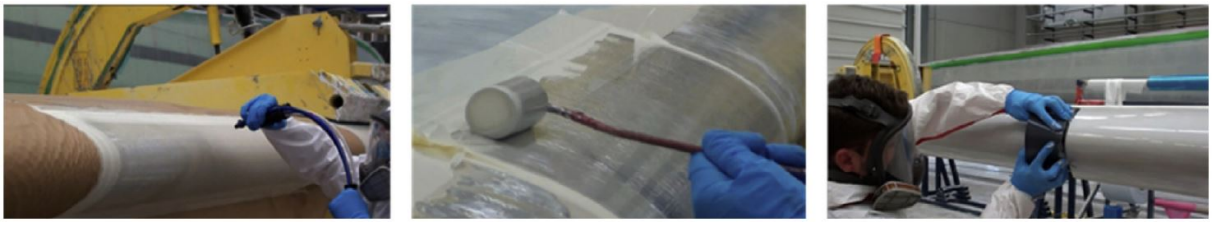

Figure 3.2: Post-mould technique for coating application. Reprinted from [41]

Flexible coatings and gelcoats present differences in their material properties. Higher values of acoustic impedance are reached for the gelcoats than for flexible coatings for example. While gelcoats are more brittle than flexible coatings who show a higher ductility. These last ones also offer high strain to failure rates. Therefore, gelcoats and flexible coatings will offer different responses to the erosion mechanisms.

3.1.1 Erosion effects on gelcoats

At the impact on the gelcoat surface, a water hammer pressure is imparted on the gelcoat surface. This in turn results in the creation of strong compressional stresses in the region of immediate contact. These initial stress values create immediate plastic damage only under extreme impact conditions. The most damaging water droplet erosion mechanism for gelcoats is the lateral jetting process where the droplet spreads across the surface at high velocity as a result of a large proportion of the impact energy being reflected into the droplet. The high pressure ring-shaped stress levels created around the impact location leads to the onset of plasticity. Therefore the vast majority of the plasticity inducement occurs on or near the gelcoat's surface while subsurface damage are very limited. Studies from Keegan [39] showed little significant different results between 60° and 90° impact angle simulations in the damage's shape but a more significant damaging at 90°.

Results from Keegan showed almost identical erosion between simulations of an epoxy based gelcoat as part of a larger glass/epoxy based composite laminate and the gelcoat in isolation with fully fixed boundary conditions on the under surface. Also delamination is unlikely to occur for gelcoats due to the inherent bonded nature of the gelcoat to the resin matrix generated during the in-mould cure

Even though the properties and characteristics of different gelcoat technologies will likely vary significantly between manufacturers and so will their impact response, the most likely form of damage of typical stiff (thermosetting resin) gelcoat material technologies will remain surface erosion.

3.1.2 Erosion effects on flexible coatings

The characteristic impact response of flexible coatings is different of that of gelcoats. Flexible coatings exhibit significant geometric deformation and a smoother impact response when subject to a range of droplet impact conditions. Therefore the likely damage mechanisms associated with such coatings also differ to those identified for gelcoats. Surface damage in the form of induced plasticity in the material was only observed in flexible coatings for the most extreme impact conditions in Keegan's work. For flexible coatings, the most significant damages were observed to occur in the subsurface regions at the interface with the coating and the respective substrate, resulting in conical distribution of material plasticity. This subsurface material degradation can lead to the weakening of the bond between the coating and respective substrate. Surface erosion may still appear, given sufficient time and/or the inclusion of other environmental exposure (such as UV) but the risk is much reduced in comparison to that associated with gelcoats.

Keegan concluded that care must therefore be taken to ensure that the bond is robust

and long lasting to avoid debonding, and thus exploit the reduced surface damage offered by flexible coatings. According to him, this debonding occurs due to the large difference in flexibility between the coating and the substrate. Similar results were obtained by Field [42] in an earlier work. The study identified that differences in flexibility resulted in intrinsic stresses in the system, often compressive in the coating and tensile in the substrate. The stresses increase the risk of debonding and can damage the substrate.

In their article, R. Herring et al. cited two other researches that agree with the previous results. Cortes et al. [41] evaluated the rain erosion resistance of an epoxy gelcoat and an elastomeric flexible coating applied over two layers of biaxial glass fibre in a whirling arm erosion test. Surface damage were stayed the main threat for the gelcoat in the form of pits and cracks while the flexible coating. Once the gelcoat had been eroded, severe delamination appeared int he composite substrate. The study concludes that flexible coatings offer better erosion protection than the more rigid gelcoats. Slot [43] states that surface fatigue best describes the erosive wear and failure of coatings and suggest to reduce this surface fatigue in order to optimise coatings. He recommends that coating development should focus on reducing the impact pressure from the rain drop and concludes that coatings have a lower modulus of elasticity should be developed. Flexible coatings having a lower modulus of elasticity, Slot does agree with Cortes' work.

3.1.3 Defects of the coatings

To be applied, a gelcoat must be first accurately mixed and applied in the mould while a flexible coating has to be applied to prepared substrate, then dried and cured. These manipulations are highly labour intensive and not automated. This has the disadvantage to lead to the appearing of many kind of defaults such as blistering, alligatoring, cracking, wrinkling, etc. The numbers of possible defects of coatings is more than significant [44]. And those manipulations become even more challenging when they are performed with repair coatings directly in the field where environmental conditions are uncertain.

Voids, blisters and areas with a lack of adhesion for example change the local acoustic impedance causing the shock waves to be reflected wherever the default occurs. Stress reflections oscillate repeatedly through the coating and substrate structure until dampened out by the material properties [41]. Defects in the composite blade also have the same effect. By reflecting shock waves back into the protection system and further loading the material, they increase the rate of erosion and lead to delamination. Slot [43] concluded from his researches that the development of coatings that present no defects and impurities is required to increase the resistance of coatings to erosion. They act as seeding points for erosion [39] causing the decrease of the lifetime of the coating. This is one of the reasons why predicting the lifetime of protection systems is complicated [43]. The defects also make it difficult to precisely schedule necessary repairs in advance and prevent further

blade damage.

To reduce the density of defects caused by the application method, the process could be automatised. Robotise different finishing processes could allow a better protection against inclement weather, ultraviolet radiation or aggression caused by erosion and mechanical bending stresses. This is because the robot can traverse the full length of the blade in a single step without stopping [45]. As the trade-off between the extra investments needed for the implementing of this technology and the savings it could provide on additional repairs (and energy losses for windmill applications) is uncertain, an economic study case should be made.

Figure 3.3: Painting robots for wind turbine blade. Reprinted from [45]

Another way to try reduce the effects of defects on protecting coatings is by developing computational models. A number of models have already been developed to attempt to estimate the expected erosion lifetime of the protection systems [43, 46, 47]. Most of these models considered a defectless adhesion between the coating and the substrate which we know, can not be assumed due to the presence of microstructural defects. A probabilistic distribution of defects produces a model closer to the reality. The second problem with computational models is that they are based on observable effects only. To increase the understanding of blade erosion and failure mechanisms in the materials, measurement of material property changes during erosion experiences would be a significant advantage. Unfortunately, it is not available and it would be limited by the strain rate capability of measurement equipment. Strain rates induced by water droplet erosion in the coatings is estimated (depending on the model) between 10^6 and 10^9. Current measurement equipment, such as Dynamic Mechanical Analysis, is limited to measurements at 10^4 and extrapolation is used to predict higher material strain rate values [4].

Erosion sensors capable of continuous monitoring of coatings are currently in development [48]. Real time property changes measurement would allow a better understanding

of rain erosion degradation processes throughout the erosion tests and validation of the results of the computational model.

3.1.4 Adhesion of the coatings

Adhesion can also reduce the performance of a protection coating. Indeed the coating adhesion and erosion is affected by the shock waves created by the collapsing water droplets on impact. Hence, indirect damage by delamination may occur at the interface boundaries between material layers, caused by the propagation and interaction of the compressional waves from the impact of water droplets, as shown in Fig. 3.4.

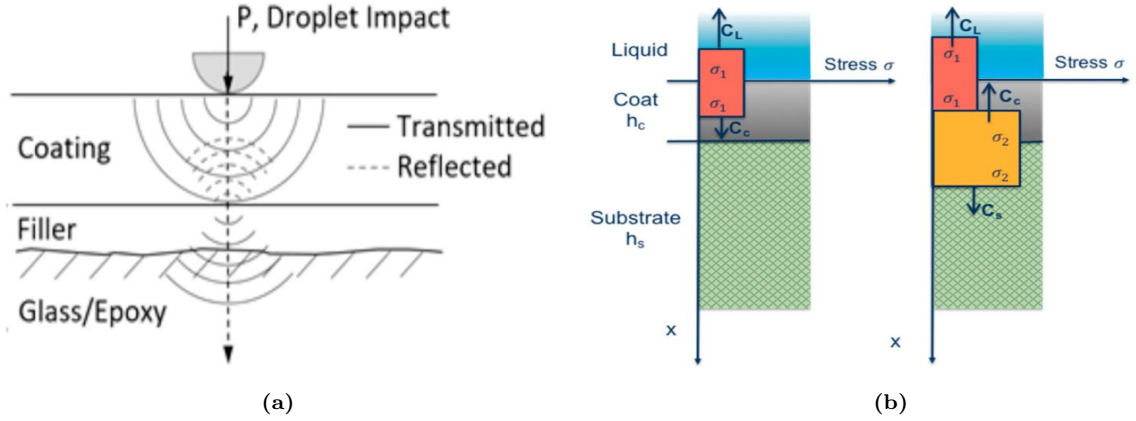

Figure 3.4: (**a**) Standard blade structure with a filler intermediate layer; (**b**) normal shock wave propagation depending on acoustic impedances in two consecutive time instants. Reprinted from [41]

A study from Cortes et al. [41] has been directed into the coating–laminate interface adhesion characterisation in order to effectively predict rain erosion performance. He first concluded that a low-modulus elastomeric material overperformed a rigid gel coating for leading edge erosion protection. A second configuration highlighted that samples manufactured with a higher degree of curing (as determined using DSC), were out-performed by those that had a lower degree of curing due to a more rigid and broad coating–laminate interface during the in-mould curing. Another set of experiments, based on the typical leading edge protection configuration, focused on the effects of including a primer layer with a filler material within a multi-layer system. It was determined that the inclusion of a primer layer drastically improves the adhesion performance between the coating and the filler substrate and consequently avoids the erosion failure by delamination. Moreover, the incubation time of the erosion damage was not appreciably affected by the inclusion of the primer layer (see Fig. 3.5).

His results highlight the importance of a strong adhesion between the coating and the substrate to achieve greater protection performance. If the adhesion is strong enough, the

failure mode will be moved into the coating instead of at the coating-substrate interface but in the other case, delamination will occur an highly accelerate erosion.

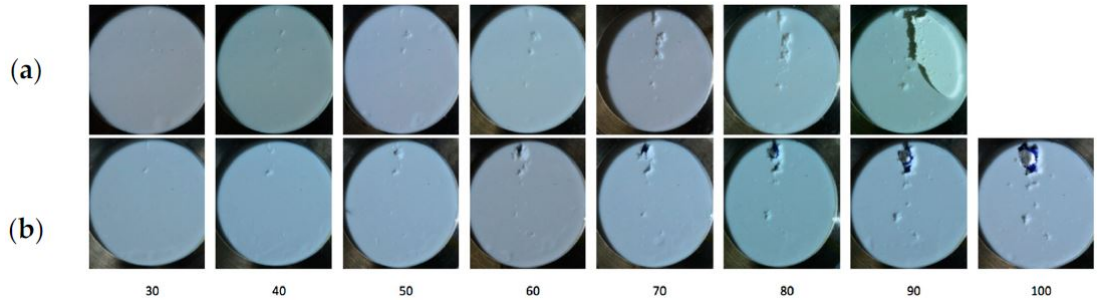

Figure 3.5: Images of surface and delamination damage after time interval (in minutes) of testing form [41]: (**a**) with no-primer application;(**b**) with intermediate primer layer.

3.2 Leading edge tapes

An alternative protection method to coatings is the post-mould application of highly flexible tapes (also primarily polyurethane based) to the leading edge of the blade. Similarly to flexible coatings, leading edge tapes have a low impedance and are ductile to dampen the initial impact of the raindrops through deformation. 3M (one of the main providers of such tapes) claims that the tapes exhibit advantageous impact, abrasion and wear properties. Fig. 3.6 compares the damage created on an unprotected bare blade and a blade protected by a Wind Protection Tape, through accelerated rain erosion testing at 500mph in a one inch per hour simulated rain field during one of their experiments at the Rain Erosion Test Facility of the University of Dayton.

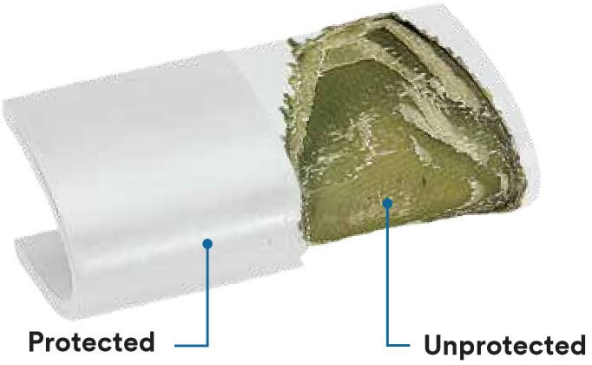

Figure 3.6: Unprotected and leading edge tape protected sample tested in rainfall of one inch per hour at 500mph at the Rain Erosion Test Facility, University of Dayton. Reprinted from [49]

The effects of leading edge tapes on defects, adhesion and aerodynamics will be discussed in this section.

3.2.1 Defects of leading edge tapes

As for coatings, the presence of defects in leading edge tapes will reduce the lifetime of the protection. Unlike the coatings, the manufacture of leading edge tapes occurs autonomously in a environment with controlled conditions and without any human interaction leading to a consistent solution with a uniform thickness and finish. This allows to reduce variability between the tapes and to reduce the average number of defects in each tape. Moreover, the application of tape is not affected by the weather conditions (unlike the one of coatings). It is therefore believed to be a more reliable solution when it comes to in-field windmill repairs [50].

3.2.2 Adhesion of leading edge tapes

The application of leading edge tapes relies on many manual procedures which make it a complex manoeuvre [51]. One of these is the preparation of a smooth and undamaged surface to assure a sufficient adhesion (a tape adhesion promoter is recommended for certain uses). Specific recommendations to avoid wrinkling, testing, bad covering and many more must be precisely followed in order to prevent the appearance of trapped air bubbles and areas of poor adhesion. Being placed in long segments, leading edge tapes could debond along the entire length of the blase if an area suffers a loss in adhesion.

The ORE Catapult (Offshore Renewable Energy Catapult) performed tests on an industrial leading edge tape [4]. An inspection of the three samples occurred before the experiment revealing the presence of air bubbles across the whole surface of samples 1 and 3, while the tape of sample 2 showed great adhesion. During the tests, intermediate check-ups highlighted that the trapped air bubbles acted as pressure points and cut through the tape. This lead to water entering and being entrapped underneath the tape. Tape detachment consequently occurred leading to the failure of both samples 1 and 3 after respectively 8h and 5h (see Fig. 3.7). Sample 2 failure happened after 11h of test due to surface damage, demonstrating again the change in failure mode from the bond to the protection solution itself in case of good adhesion.

Figure 3.7: Significant tape detachment and water entrapment in sample 1 after 8h and in sample 3 after 5h of rain erosion testing. Reprinted from [4]

In Keegan's work [39], the adhesion limit was defined using the following interface failure criterion :

$$\left(\frac{|\sigma_n|}{NFLS}\right)^2 + \left(\frac{|\sigma_s|}{SFLS}\right)^2 \geq 1 \ , \tag{3.1}$$

where σ_n and σ_s are the normal and shear stresses acting on the interface respectively, and NFLS and SFLS are the normal and shear interlaminate strength values respectively. Its use can be complicated as there is limited publicly available data on the strength and characteristics of the typical bond between tape and the substrate. His experiences showed that tapes exhibit levels of deformation that far exceed those exhibited by gelcoat (by multiple orders of magnitude). The tape responds to the initial droplet impact in a comparatively flexible manner, compressing heavily in the direction of impact and re-

ducing heavily the maximum effective stress that appears in the protection solution (see Fig. 3.8).

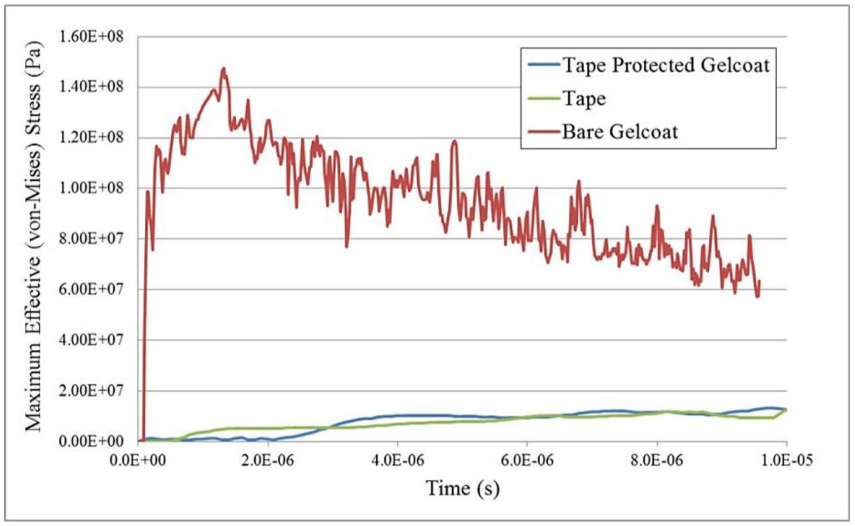

Figure 3.8: Time history of the maximum effective stress in an unprotected gelcoat and a tape protected gelcoat and attached tape material, for a 3mm diameter water droplet impact event, with 100m · s-1 impact velocity. Reprinted from [39]

He concluded that the typical impact response of the protective tape modelled was very similar to that exhibited by the previously modelled flexible coating; as would be expected, given their comparative material properties. Tapes also show less surface erosion and degradation than gelcoats but the most likely damage mechanism with tape technology is subsurface plasticity and material degradation at the tape-substrate interface (as for flexible coatings). Therefore, the biggest threat is posed by interlaminate pressures and forces that could damage the bond between tape and substrate surface, especially as tapes are often applied to operational blade surfaces which have already exhibited damage. The better erosion resistance of leading edge tapes is thus not fully exploited but an enhancement of the application processes (with automatisation) may provide a breakthrough by achieving consistent robust bonds.

3.2.3 Aerodynamics of leading edge tapes

The larger thickness of leading edge tape compared to coatings has its advantages but one of the downsides is that it protrude from the leading edge (3 mm thick following 3M application guide [51]). In 1999, Giguère and Solig [52] analysed the aerodynamic effects of leading edge tape on aerofoils. During their research, the tape was shown to trigger early transition to turbulent flow, and the resulting effect on drag depended on the trade-off between bubble, device and skin friction drag. Therefore the magnitude of the aerodynamic effects caused by the tape is aerofoil-dependent. The losses in power

coefficient increased rapidly with the number of tape layers and Reynolds number. They also listed some application guidelines :

- The chordwise extent of the tape on the pressure surface can be selected according to the expected impingement limits, because it was found to have negligible effect on aerofoil performance.

- Unless turbulent flow aerofoils are used, the location of the tape edge on the section surface (or upper surface see Fig. 3.9) has a much larger effect on aerofoil performance compared with that on the pressure surface (or lower surface). Ending the tape relatively close to the leading edge, such as 5% chord, should be avoided as it typically reduces aerofoil performance. Aerodynamically, a better option is to extend the tape to 15%-30% chord. Therefore protecting a larger portion of the suction surface with tape results in a smaller reduction in aerofoil performance.

- When multiple layers of tape are used, which is typical for the outboard section of the blades, it is preferable to stagger the layers over ending them at the same location.

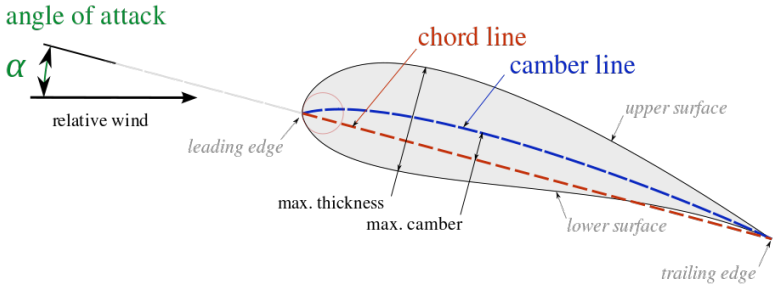

Figure 3.9: Wing profile nomenclature. [53]

Keegan uses research from Chinmay [54], which found that implementing leading edge tapes on aerofoils resulted in a drag increase ranging from 5-15% - depending on placement and area size - and although this may not result in a measurable difference in annual energy production, research would be required to determine the optimal method of application to minimise any detrimental aerodynamic effects. By using tape on a full scale commercial turbine tip, Kidder [55] measured a loss of 20% in drag and a loss of 25% in lift at low angles of attack but the impact to drag and lift reduced at high angles of attack. They both agree that the use of tape has an influence on the aerodynamic of a tape but not a critical influence. However, the effect of the slightly unfavourable aerodynamics on the turbine loading and fatigue are unclear [4]. According to Guigère and Solig, these potential issues could be alleviated using thinner tapes but that would also reduce the main purpose of leading edge tapes. But the according to Herring et al.

[4], the minimal losses in performance is likely offset by the protection provided by a wall applied tape.

3.3 Erosion shields

Another solution that has recently begun to develop is what is called *erosion shield*. It consists of applying highly durable covers to the leading edge in modules. The manufacture takes place in controlled production environments to minimise the number of defects (as with leading edge tapes) where they are affixed in a single piece, or shorter dovetailed pieces, using adhesives (thereby avoiding wrinkling issues during the application). Erosion shields can be rigid or semi-flexible but tend to be thicker than coatings and tapes, allowing to further expand and dissipate the raindrop shock wave, reduce the damage transferred to the rigid composite blade and move any voids int he blade substrate further from the shock waves [4]. However, the interfacial stresses between blade and shield, that may be caused by differences in flexibility and rigidity during the blade operation, could lead to the adhesive breakdown and the shields debonding from the blade in the most severe cases.

According to Herring et al, as erosion shields are manufactured ready to be positioned straight onto the leading edge, they can have their shape tailored for specific blades. This ensures a near perfect fit and results in only marginal modifications to the geometry of the blade. This makes erosion shields initially more expensive, however, should it alleviate the effect of leading edge erosion, they could represent a better return on investment to turbine owners. This will become apparent as the technology develops and becomes widely utilised.

AmourEDGE [56] produces such a shield from extruded sheets of a tough thermoplastic. Instead of resulting in large pits when they erode, thermoplastic materials provide a smooth removal of the material, causing less aerodynamic losses. Adhesive is applied to the underside of the erosion shield then distributed using a bespoke spreader design, the shield is then aligned with adjacent shields to ensure an aerodynamically optimal surface and pressed into place. The tapered edges of the shield are then faired in further to the leading edge surface to create a smooth transition. Finally, a protective coating may be applied to protect the joints from environmental factors. The efficiency of this solution is suspected to be reliant on the quality of the adhesion, care must therefore be taken that the bond between blade and shield is strong.

The helicopter industry has already been using erosion shields for a few years. Following Weigel's study [57], it seems that metals outperform polyurethane materials (typical materials of flexible coatings and leading edge tapes). It explains why metallic shields, typically composed of stainless steel, nickel or titanium, are used as rain erosion protection

for helicopter leading edge blade [58]. However regular inspections of the adhesion quality need to be performed on the air crafts as maintaining adhesion in service can be an issue with erosion shields. For windmill applications, this could represent an important issue due to the difficulty to orchestrate such an operation of a turbine in service. On the other side, it will be less harmful for aerospace applications.

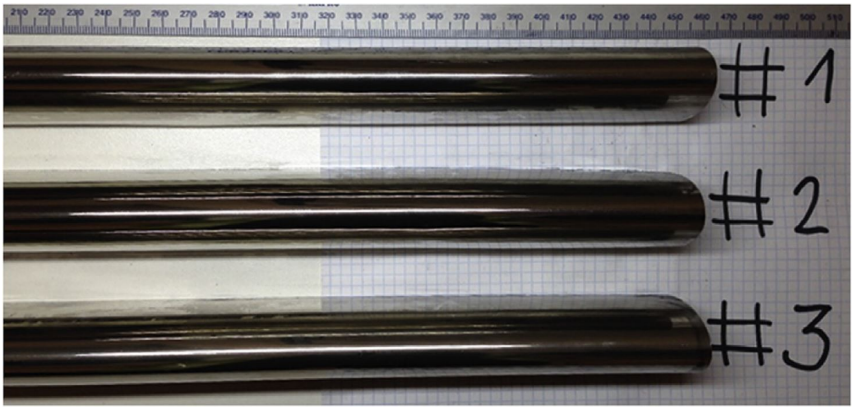

Figure 3.10: Nickel alloy sample after 85 h of rain erosion testing at a rotational speed of 173 m/s. [4]

As metals have an higher impedance than typical gelcoats [43], a larger part of the droplet impact energy will be reflected and the jetting across the surface will be larger too. This can be counteracted with a smooth surface and a high hardness that resists plastic deformation but surface degradation will remain the main damage source for erosion shields. Indeed, the shield-blade interface and bond degradation are unlikely to appear first as the higher impedance causes a smaller proportion of droplet energy to be transferred. This resistance allows certain metallic shields to have excellent rain erosion performance at higher tip speeds than seen for polymeric materials. Results of a rain erosion test on a nickel alloy sample presented by Herring et al.[4] showed no surface degradation after 85h at rotational speeds of 173 m/s (see Fig. 3.10).

3.4 Integrated erosion shields

To try to enhance the adhesion of the shield, the adhesive bonding between shield and blade could be replaced by co-bonding or co-curing the shield directly into the blade. By turning the adhesion process into an in-mould manipulation, the lifetime of the protection solution could potentially be increased while reducing the manufacturing steps required for current post-mould solutions.

- **Co-curing :** The act of curing a composite laminate and simultaneously bonding it to some other uncured material, or to a core material [59]. The composite will be directly cured onto the shield and form a mechanical bond between its matrix and the shield. The excess resin, extracted during consolidation of the composite,

provides the adhesion between the shield and the composite [60], allowing to remove the adhesive from the bond. A suitable resin must be chosen in order to ensure a robust bond with the shield and consolidation of the composite.

- **Co-bonding :** The curing together of two or more elements, of which at least one is fully cured and at least one is uncured [59]. The adhesive and the composite will be cured during one single cycle to reduce the post cure thermal stresses experienced by the composite. It does require careful surface preparation of the shield [59]. A mechanical bond is created between the adhesive and the metal and a strong chemical bond between the adhesive and the matrix material of the composite. However, there are two distinct interfaces, a mechanical and a chemical bond. Therefore care must be taken to ensure a suitable adhesive is chosen to form robust bonds with both the shield and composite [61].

Combining the attachment of the shield into the curing of the blade itself would require only one mechanical bond between the shield integration, as opposed to two in post-mould adhesive bonding. The process would also negate both the need for and time required of an additional manufacturing step, as well as ensuring a smooth exterior to the blade, with no step in the profile where the shield is included [4].

3.5 Discussion

A resume of the different protection solutions categories has here been presented and their main characteristics discussed. Some key advantages and disadvantages were presented. All the protection solutions have common failure issues. A summary of the protection solutions presented hereinabove is available in Table 3.1.

Coatings, being applicated in-mould or post-mould, gelcoats or flexible coatings, are manually applied to the blade, increasing the appearance rate of defects and therefore the erosion rate. The autonomous manufacture of leading edge tapes placement makes its relatively risk-free. But with the slightest defect, the adhesion will largely decrease due to the appearance of wrinkles and air pockets. Tapes will absorb the impact energy better due to its low impedance but will fail by subsurface degradation causing the debonding of the tape. The mechanism will accelerate in areas that show reduced adhesion.

The manufacture of erosion shield is also autonomous and in a controlled environment. Moreover, they can be tailored to each blade assuring a better fit due to the minimised amount of discontinuities. The wrinkling risk almost disappears thanks to their greater rigidity. They showed excellent erosion resistance in the helicopter industry as in rain erosion tests. Their high impedance forces the appearance of erosion damage at the surface, reducing the importance of adhesion. However, due to creep and structural loading, long term resistance of the adhesion remains a question.

Protection Solution	Application	Susceptible to defects	Susceptible to poor adhesion	Aerodynamic issues	Debonding risk	Average erosion resistance
Gelcoats	In-mould	Yes	No	No	No	Poor
Flexible coatings	Post-mould	Yes	Yes	No	Yes	Medium
Leading edge tapes	Post-mould	No	yes	Slightly	Yes	Good
Erosion shields	Post-mould	No	Potentially	Potentially	Yes	Very good
Integrated erosion shields	In-mould	No	No	No	Yes	Excellent

Table 3.1: Simplified summary of the existing protection solutions. Reprinted from [4]

In the second part of this thesis, erosion tests will be performed under different conditions and with different materials. The acquired knowledge will be useful to determine which tests need to be conducted and which variables analysed.

Part II

Water Droplet Erosion Tests

Chapter 4

Water droplet erosion experimental tests

At the beginning of this thesis, the objective of the experimental part was to use the test bench developed at the UCLouvain. A rotating test bench which would better simulate erosion of airplanes or windmills since the samples are rotating at high speeds and intercepts the trajectory of vertically falling droplets (in comparison with most erosion test benches where water is projected at high speeds on motionless samples).

4.1 Description of the test bench

To analyse degradation due to erosion occurring on composite materials due to repeated impacts of water droplets, a test bench has been developed at UCLouvain.

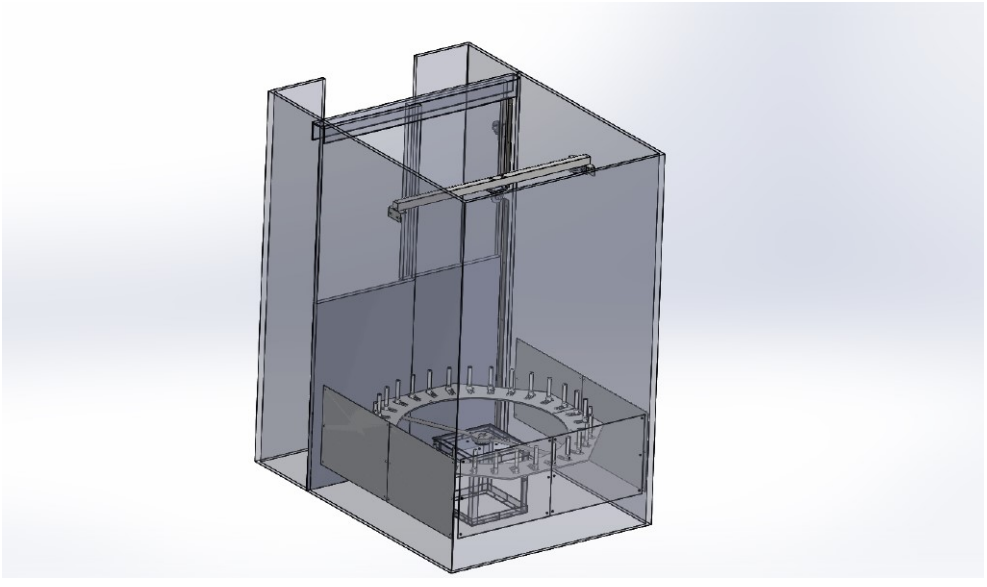

Figure 4.1: CAD model of the erosion test bench

As described by Masson [62]: "It consists of a double-rotating arm mounted on a motor case inside a dedicated room. The room is a local inside the UCLouvain facilities and is a closed rectangular room of 1.8 × 1.8 meters and 3 meters high. A separation

sliding door and wall protections are placed around the arm in case of any mechanical failure. The water injection mechanism will work as follows. A reservoir will feed water to syringes that are piercing through the plug of protecting tubes. Those tubes will protect the water injection at the tip of the syringe to allow the formation of a water droplet. The tubes are mounted in adjustable slots on an octagonal support. This support is attached to the ceiling with a system of pulleys that allows the adjustment of its height.

The arm and the sample holder are presented in Figure 4.2. This double arm has a diameter of almost 1.61 meters. The sample is a small circular sheet of material whose center is located at a radius of 0.785 meters and has a diameter of 28 millimeters. It is inserted in the open orifice in front of the sample and is held in place by a spring pressing it against the small edge.

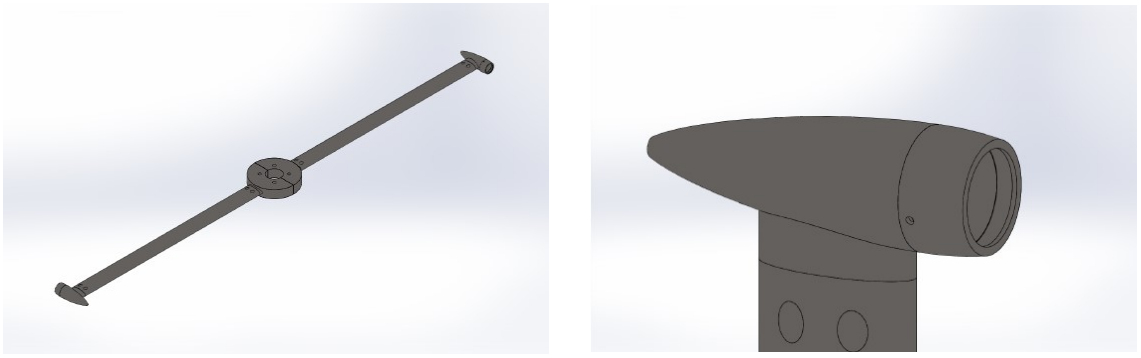

Figure 4.2: CAD model of the arm and sample holders

A closer look at the motor case and the injection mechanism is taken in Figure 4.3. The motor case is 51 centimeters high, 52 centimeters wide and is fixed to the ground. The arms will be mounted on top of it with the appropriate bearing, and inside it will be an electric motor. The injection mechanism is composed of two plates that are held together. The final shape is an octagonal exterior limit with 70 centimeters edges and a circular inner limit with a radius of 62.5 centimeters. There are 32, 13 centimeters long, slots evenly distributed around the circle. In each slot an injection tube of 20 centimeters high and 28 millimeters in diameter can be mounted. Since the support is mounted to the ceiling by a pulley, its height in the room is adjustable. This also has the added advantage to insulate it from the electrical motor and reduce the vibrations. This will help to ensure a good formation of water droplets.

To match the required investigation velocity the arms will rotate at 2190 rpm. This rotation speed allows the center of the samples to evolve at a tangential velocity of 180 m/s. The water droplet injection mechanism is designed to produce water droplets with a diameter of two millimeters. The testing sessions can last as long as water is injected and the arm is rotating."

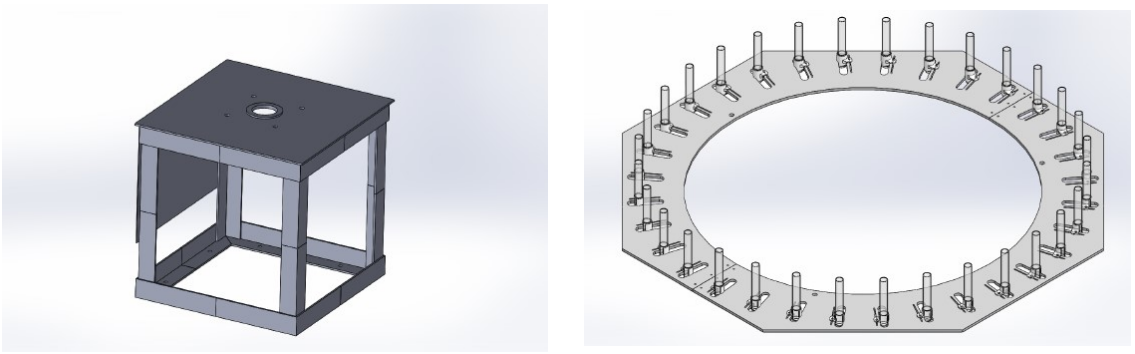

(a) Motor case

(b) Complete injection mechanism

Figure 4.3

4.2 Experimental method

Following this guideline, we updated the test procedure so that it meets the updated version of the test bench (cf. Appendix A). Unfortunately, due to the appearance of the COVID-19, causing the shut down of the laboratories and difficulties to meet, we had to switch our analysis from experimental tests to numerical simulation.

Chapter 5

Water droplet impact numerical simulation

5.1 Model

To replace the real life experiments, we decided to switch from real-life experiments to numerical experiments. In order to create a model for our water droplet erosion problem, a static finite element approach is used that was proposed at the University of Grenoble to model the pits in walls due to repeated collapse of cavitation bubbles [63] [64].

The finite element analysis software *Abaqus* developed by *Dassault Systèmes* is used to implement our model. Throughout all our numerical developments, we considered standard conditions of temperature (T= 20°C) and pressure (p = 1 atm).

5.1.1 Finite element model

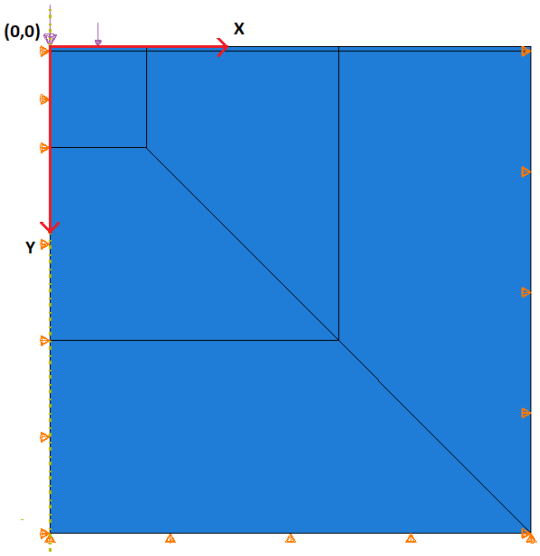

Figure 5.1: General view of the model used

Erosion is a complex phenomenon that involves a lot of solicitations of different natures. With our knowledge in *Abaqus* and the time available, precisely modelling every damage mechanism was not an option. The focus was put on the first mechanism. Indeed by delaying direct deformation, the impact of the other mechanisms will decrease. It was decided to implement the load of the droplet and the pressure that it generates on the solid surface and study how the stresses propagate inside the solid.

Sample

An axisymmetric model is used as proposed by Roy et al. [63] and Fivel et al. [65]. The size of our part is chosen by adapting it to the scale of the other elements (droplet size, coating thickness) while having enough under-surface depth to observe the stress propagation in the solid. Our sample's final size is a 1cm x 1cm axisymmetric square, represented in Fig.5.2b.

Mesh

The mesh is divided into 3 regions. The first one with a very fine square mesh with equally spaced nodes, near the center of the droplet impact (located at the top-left corner (0,0)). The second region has a slightly more coarse mesh and the nodes are spaced using a bias in order to use less elements as we move further for the impact point. The third region (at the bottom and the right of the element) has a relatively coarse mesh. By using 3 regions, we can get very precise data near the impact point without having to support too much nodes in the less-interesting region.

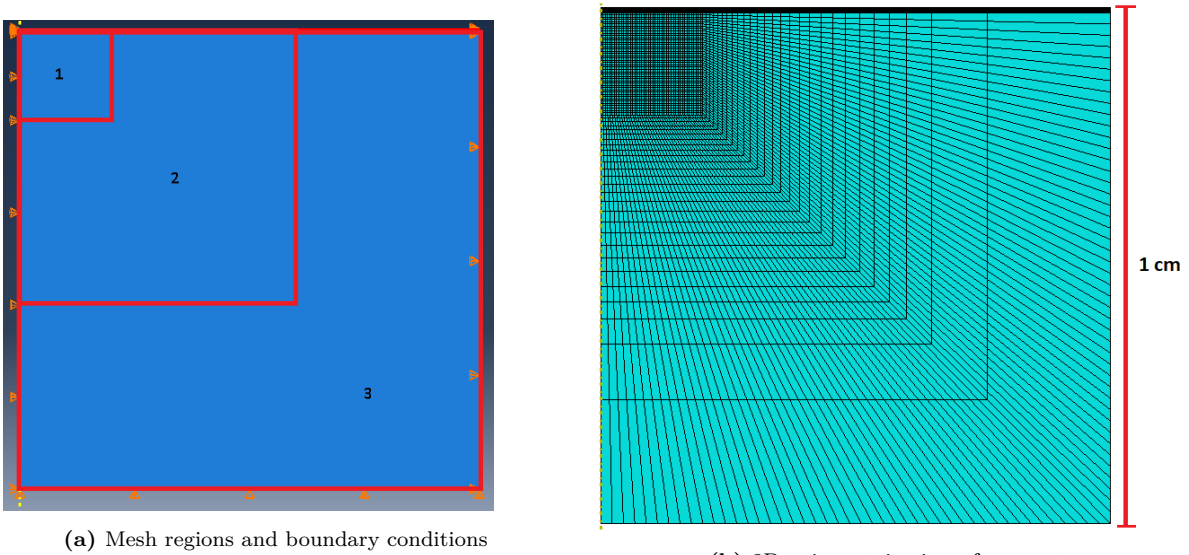

(a) Mesh regions and boundary conditions

(b) 2D axisymetric view of our part

Figure 5.2

Quadratic finite elements are used to increase the interpolation quality between nodes and it fits our model geometry nicely.

In order to select the number of elements of the mesh, we focused on two values : the total amount of energy (in joules) and the maximum displacement (in meters) obtained at the end of the simulation. These values are plotted as a function of the number of finite elements used for the calculations, as represented in Fig. 5.1.1.

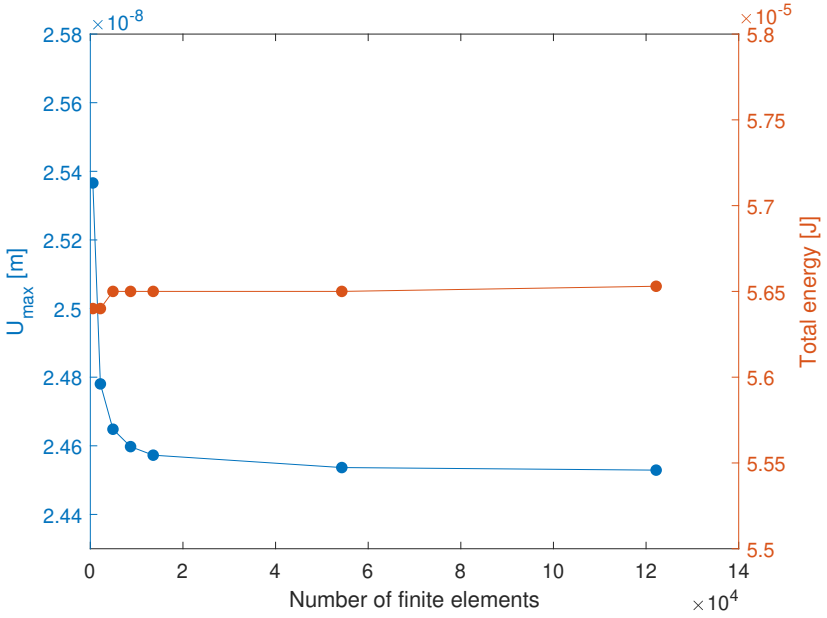

Figure 5.3: Influence of the mesh size

The total energy does almost not vary with the mesh size. On the other hand, the value of the maximum displacement, that will be of main interest, converges with the increasing mesh density. We choose for our simulations a mesh size between 5175 and 6255 elements, depending on the thickness of the coating. Using this mesh size, we observe a reasonable <1% error compared to the 120 000 elements mesh with a computation time around 10 minutes.

Boundary conditions

Boundary conditions were implemented on 3 faces of our element, letting the top surface free of any movement. The left and right sides are blocked in the horizontal direction since there is matter in those directions that will counteract and the bottom surface cannot move vertically for the same reason. Tests without the left an bottom boundary conditions showed negligible variations because the effects of the droplet impact are almost null this far from the impact area.

5.1.2 Liquid-solid impact

The impact of a droplet is implemented as a pressure field with its magnitude being linked to the peak value of the water-hammer pressure mentioned before. This pressure will be maximal at the impact point and decreasing moving away from this point as represented in Fig. 5.4 with σ_H the peak pressure of hydrodynamic impact, r the distance from the origin (0,0) and r_H the radial extent of hydrodynamic impact. For this last one we had to make an approximation since we do not have a relation for the values of r_H in the case of erosion. We took $r_H = 1\ mm$ which is the radius of the droplets created for the bench test (typical diameter of droplets encountered for rain erosion is 1-5 mm for aircraft and 0.5-5 mm for wind turbines [14]) and which should be close to the radial extent of the impact.

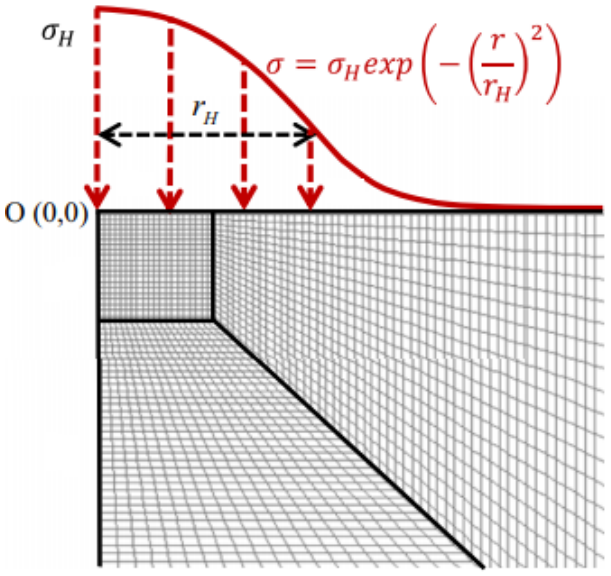

Figure 5.4: Loading region and stress distribution. Reprinted from [63]

For the peak pressure σ_H we used the approximation from equation 5.2 given in [14]:

$$\sigma_H = p_{max} = 3\ p_{WH}\ , \tag{5.1}$$

where the water-hammer pressure p_{WH} is given by :

$$p_{WH} = \frac{\rho_0 C_0\ \rho_s C_s\ V}{\rho_0 C_0\ +\ \rho_s C_s}\ , \tag{5.2}$$

where the subscript *0* corresponds to the water and the subscript s to the material impacted by the water droplet. The pressure applied will consequently depend on the material impacted (for different coatings) and the speed of the impact.

Droplet parameters	
ρ_0	1000 kg/m^3
C_0	1430 m/s
r_H	1 mm

Table 5.1: Consistent parameters for droplet impact simulation

5.1.3 Cyclic loading

The load of the water-hammer pressure is implemented as a static load with a certain duration. Since our simulation only models the direct deformation mechanism of erosion, it would be useless to run the test for thousands of impacts, like it is done during experimental erosion tests. The main focus is the action of one single impact on the solid and to determine the best materials and conditions to lower the effects of that impact and by doing so, retarding the high damage mechanisms that are lateral jetting and hydraulic penetration.

Even though one single droplet would allow us to understand the stress propagation in the solid, we still did run the test for a few droplets in order to see the hardening of the material and to see the evolution of the residual stresses between each impact.

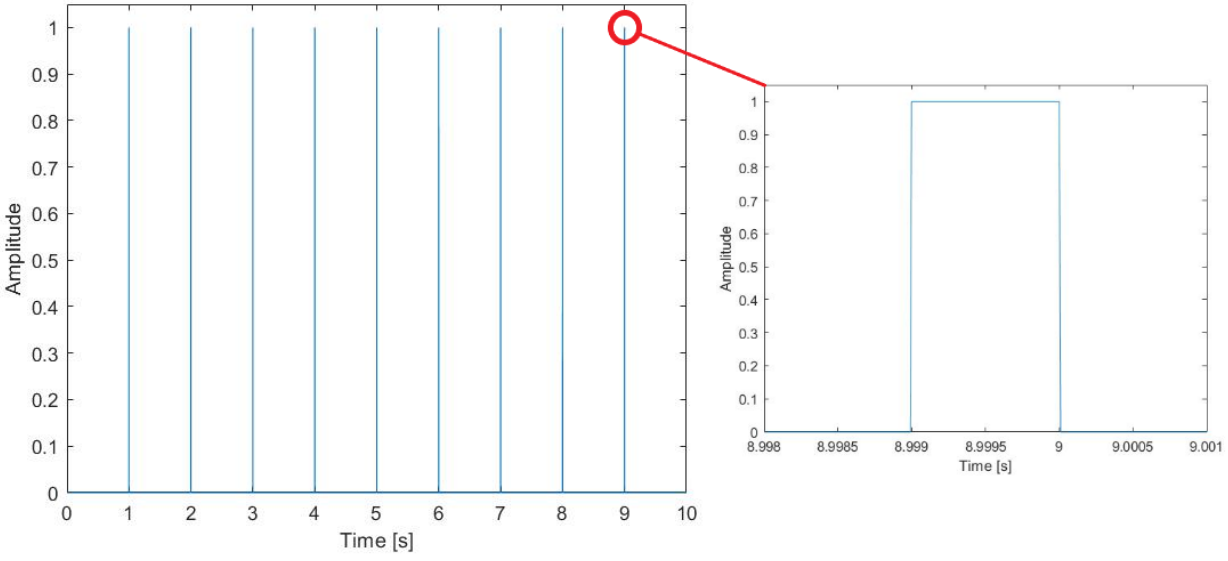

Figure 5.5: Amplitude of load of the peak water hammer pressure over time

The element is hit by 9 water droplets in a 10 seconds period of time. We chose to let the element at rest for 1 second to see its behaviour with no charge but since our model assumes an instantaneous unloading, this choice is purely arbitrary. Each droplet

is modelled as a 1 millisecond pressure on top of the solid. This is implemented as a varying amplitude of the load over 10 seconds, as represented in Fig. 5.5.

5.1.4 Material properties and constitutive models

To model materials and their mechanical properties in *Abaqus* is a challenge that varies in difficulty depending on the type of materials and the experiments you want to conduct. We can divide the materials used for our erosion tests in different categories base on the model implemented. The model for each of these is described here under.

Metals

Metals are taken as elastically isotropic materials, the density (ρ) and the elastic behaviour (E and ν) are easy to implement . The interesting part is the plastic behaviour and more importantly the hardening mechanism as a function of strain. We thus use the J2 plasticity model where 2 stress-strain equations are added to define the elastic-plastic behaviour of metals: the classic elastic relation (5.3) for stresses below the elastic limit and for the plastic strains, Hollomon's law (5.4) using a constant multiplier and an exponent.

$$\sigma = E\,\epsilon \quad \text{for} \quad \sigma < \sigma_y \ , \tag{5.3}$$

$$\sigma = K\epsilon_p^n \quad \text{for} \quad \sigma_y < \sigma < \sigma_u \ , \tag{5.4}$$

where σ is the true stress, ϵ the true strain, ϵ_p the plastic strain, K the hardening constant, n the hardening exponent and σ_y and σ_u respectively the yield stress and ultimate stress of the material.

The J2 plasticity model is an elastic-plastic model with isotropic hardening based on the von Mises yield function with associated flow rule and also the most common model in numerical plasticity analysis of metals. The standard J_2-plasticity model with linear hardening model implemented in FEM and Newton-Raphson algorithm is able to simulate the material response up to the turning point from hardening to softening (= the point where the slope of the stress-strain curve reaches zero).

The common name "J_2 plasticity" given for the von Mises theory is prompted by the fact that it is described in terms of the second invariant of deviatoric stress, J_2 [66] [67] :

$$\begin{aligned} J_2 &= \frac{1}{2} s_{ij} s_{ij} \\ &= \frac{1}{6}[(\sigma_{11}-\sigma_{22})^2 + (\sigma_{22}-\sigma_{33})^2 + (\sigma_{33}-\sigma_{11})^2 + 6(\sigma_{12}^2+\sigma_{23}^2+\sigma_{31}^2)] \ , \end{aligned} \tag{5.5}$$

where s_{ij} are the components of the stress deviator tensor σ_{dev}

$$\sigma_{dev} = \sigma - \frac{1}{3}\,\mathrm{tr}(\sigma)\ \mathrm{I} \ . \tag{5.6}$$

The von Mises yield criterion states that a stress tensor is at yield if

$$J_2 = k^2 \ , \tag{5.7}$$

where k is a positive material constant. It can be found running a shear stress test ($k = \tau_y$) or an uniaxial tensile stress test ($k = \frac{\sigma_y}{\sqrt{3}}$). If $J_2 < k^2$ (*resp.* $>$), the material is treated as elastic (*resp.* plastic).

The data for the metals simulated in this work can be found in Table 5.2.

Material	ρ [kg/m^3]	c [m/s]	E [GPa]	σ_y [MPa]	σ_u [MPa]	ϵ_{max} [%]	K [MPa]	n [-]
Aluminium 2024-T3 [68]	2780	5100	73.1	345	483	18	690	0.16
Nickel-Bulk [69]	8890	4970	207	114	425	24.35	737	0.39
Nickel-PED21 [69]	8890	4970	207	1228	1474	3.95	2006	0.093
Nickel-PED42 [69]	8890	4970	207	766	1058	5.88	1422	0.1
Nickel-PED70 [69]	8890	4970	207	440	648	8.8	873	0.123
Nickel-PED195 [69]	8890	4970	207	334	512	13.09	720	0.164
Titanium Ti6Al4V [70]	4430	4140	113.8	950	1050	14	1150	0.04

Table 5.2: Material properties of metals

The Al2024-T3 is the most commonly used aluminium alloy to date for aircraft applications. The different Ni-PED are pulsed electrodeposited nickels, PED70 meaning that the grain size is 70 nanometers. Bulk nickel is not electrodeposited and the grain size is around 43 000 nanometers [69]. Ti6Al4V is a titanium alloy also used for aircraft applications.

Before entering anything in *Abaqus* you must pay attention the program requires the *true stress* and the *true strain* in order to interpret the data correctly. But while most experimental stress-strain curve are expressed in nominal (or engineering) stress and strain, Hollomon's law already uses true stress and strain.

Elastomers

To model polyurethane-based leading edge elastomer tapes, we implemented an hyperelastic-viscoelastic model as done by Fallon & McShane [71]. The goal is to obtain a representative model of a realistic elastomer coating to allow subsequent interrogation and not to obtain an exact match of a particular coating.

First, hyperelastic parameters were added to the *Abaqus* model. We therefore used the compression test proposed by Fallon & McShane at a strain rate of $10^{-3}s^{-1}$ to get a realistic elastomeric response that we then extrapolated to match our model's load and strain. They found out that the Yeoh strain energy potential gave the best fit and

implemented a nearly incompressible variant of it, corresponding to a Poisson's ratio of $\nu = 0.475$. More info on its formulation can be found in [71].

In addition, a Prony series was used in conjunction with this hyperelastic model to provide a viscoelastic behaviour. The Prony series parameters used come from Mauchien [72] and are presented in Table 5.3.

n	$\overline{g_n}$	$\tau_n(s)$
1	0.94159	1.49E-6
2	1.31E-2	2.93E-5
3	1.01E-2	2.79E-4
4	7.62E-3	3.02E-3
5	5.69E-3	3.77E-2
6	4.17E-3	0.55586
7	3.01E-3	10.035
8	2.13E-3	236.29
9	1.43E-3	7521

Table 5.3: Prony series parameters for elastomer model [72]

CFRP

CFRP is the most used class of composite material for the structure of air planes. The material properties vary depending on the type of the composite. There are two main configurations namely unidirectional and woven carbon fibers. The unidirectional is widely used in practice and in research and therefore has been extensively covered in literature.

Elastic properties	
E_{xx}	127.40 GPa
E_{yy}	9.91 GPa
E_{zz}	9.91 GPa
ν_{xy}	0.30
ν_{xz}	0.30
ν_{yz}	0.44
G_{xy}	4.73 GPa
G_{xz}	4.73 GPa
G_{yz}	3.52 GPa
ρ	1600 kg/m^3

Table 5.4: Average values of the different engineering constants used in the studies listed in [73].

Properties of composites are direction dependent which is why elastic anisotropic material specifications are used in FE analysis. The anisotropic properties indicated hereinabove were computed as the average of the properties found in six other studies as listed in [73]. The fibers are set along the x axis (parallel to the impacted surface).

5.2 Model limits

When implementing a numerical model, it is impossible to take all the parameters into account. Therefore, simplifications were made and it is needed to have them in mind when interpreting our results. In the previous sections, we already discussed the limitations caused by the mesh, the constitutive models of the materials and the implementation of only the direct deformation, first mechanism of erosion. Here under, are some other limitations of the model to keep in mind.

Static approach

The static nature of the model is one the biggest limit of our analysis. We cannot observe the shock wave propagation and how they would interact with the interface or the boundaries of the sample after the impact.

We do not take into account the dynamic aspects such as the sound of speed and density increase in the liquid, the inertial effects, the kinetic and hydrodynamic aspects, influence of the impact duration, etc.

Interface modeling

The coating-substrate interface from our model is a perfect interface. Therefore the transition of the different output variables (stress, strain, displacement, etc.) only depends on the change of the material properties. Debonding will hence never occur due to the infinite adhesive and cohesive strengths.

Therefore the adhesive strengths of different adhesion enhancement solutions such as electrodeposition, adhesives, mechanical bonding, use of a primer layer, etc. will not be discussed throughout this work.

Strain rate dependence of materials

The only time-dependent material responses that can impact a static analysis are rate-dependent yield, hysteresis and viscoplasticity [74]. The rate-dependent yield would have a non-negligible impact on an water droplet erosion analysis due to the high strains observed in the coating systems. Current models predict strain rates between 10^6 and 10^9 for rain impacts [4].

In our analysis, we did not implement any strain rate dependence for the metals and

the CFRP. For the elastomer we tried to adapt values of compression stress-strain tests found in other studies to our case. In order to improve the strain rate dependence, our own tests should be performed at the desired strain rates.

Residual stresses

The computation of residual stresses in the model shows some errors (up to a few MPa) when no plasticity was reached since we are in a load/pressure control. The locally applied pressure creates a non-uniform stress field in the sample. Then by going to a forced zero load almost instantaneously, some residual non-uniform displacement and stresses maintain (while having a zero net force on your upper boundary). In the case of an uniform pressure applied at the top instead of our local pressure at the top left corner, these errors in residual stresses were only of a few Pascals.

Nevertheless, the materials that will really be subjected to erosion, will also be subjected to residual stresses. For instance, adhesion techniques such as electrodeposition will most certainly create some internal stresses even before the erosion starts. Therefore, depending on the order of magnitude of the residual stresses obtained for each simulations, conclusions should be taken only if these errors are considered negligible.

5.3 Results and discussions

We started our analysis with the observation of the typical response of two different types of coatings, metallic and elastomeric, hit by the same droplet. These first tests were performed under reference conditions based on common tests. The reference impact velocity V is 180 m/s, *i.e.* the velocity the company *Sonaca* uses to perform erosion tests. The reference coating thickness is 100μm for the metallic coatings and 450μm fir the elastomeric coating.

Based on these observations we will be able to compare further results obtained by varying different parameters. Fig. 5.6 shows an axisymmetric view of the maximum principal stresses in an aluminium substrate with a titanium coating in (a) and an elastomer coating in (b) at the moment of the impact. Positive (*resp.* negative) values of stresses represent tensile (*resp.* compression).

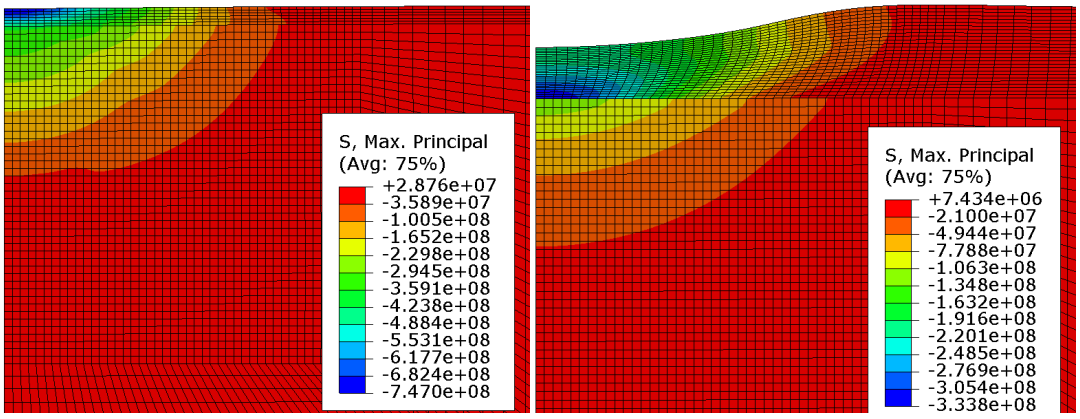

(a) Standard titanium coating, at impact **(b)** Standard elastomer coating, at impact

Figure 5.6: Maximum principal stresses (in Pa) at impact on Aluminium 2021-T3 substrate

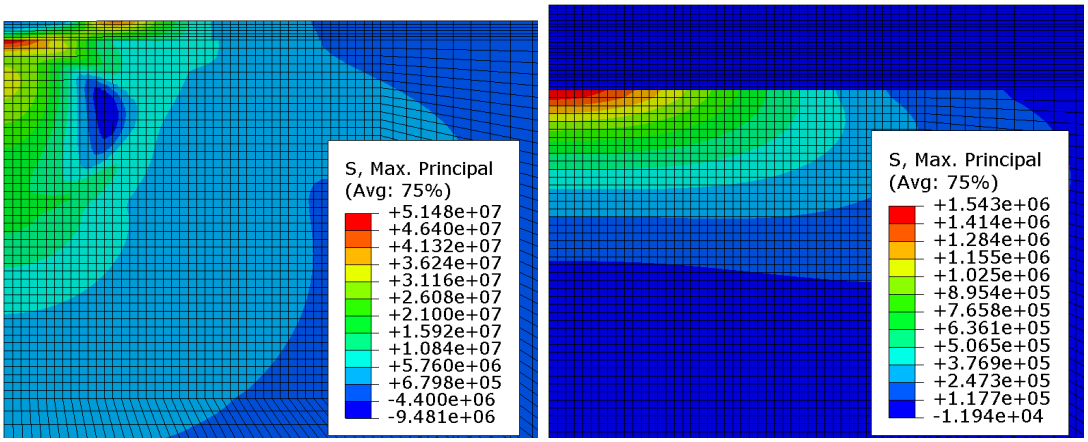

(a) Standard titanium coating, after impact **(b)** Standard elastomer coating, after impact

Figure 5.7: Maximum principal stresses (in Pa) after impact on Aluminium 2021-T3 substrate

Concerning the distribution of maximum principal stresses (Fig. 5.6), the titanium coating (here on an aluminium substrate) shows an almost continuous stress field with the maximum compressive stress situated at the impact point, decreasing with distance in both axial and radial direction. On the other hand, the elastomer coating shows a different behaviour. The maximum compressive stress is located deeper in the coating, at the interface with the substrate. Due to their lower modulus and viscoelastic behaviour, elastomers are able to dissipate the shock wave and the impact energy, resulting in stresses of lower magnitudes than in harder and more rigid materials such as metals.

Therefore residual stresses (after unloading) are also lower in the aluminium substrate when covered by the elastomer coating, see Fig. 5.7. However the stresses discontinuity at the interface is lower when the titanium coating is applied. Another information worth mentioning is the fact that our model always gives the material time to fully recover (which would be faster for the elastomer).

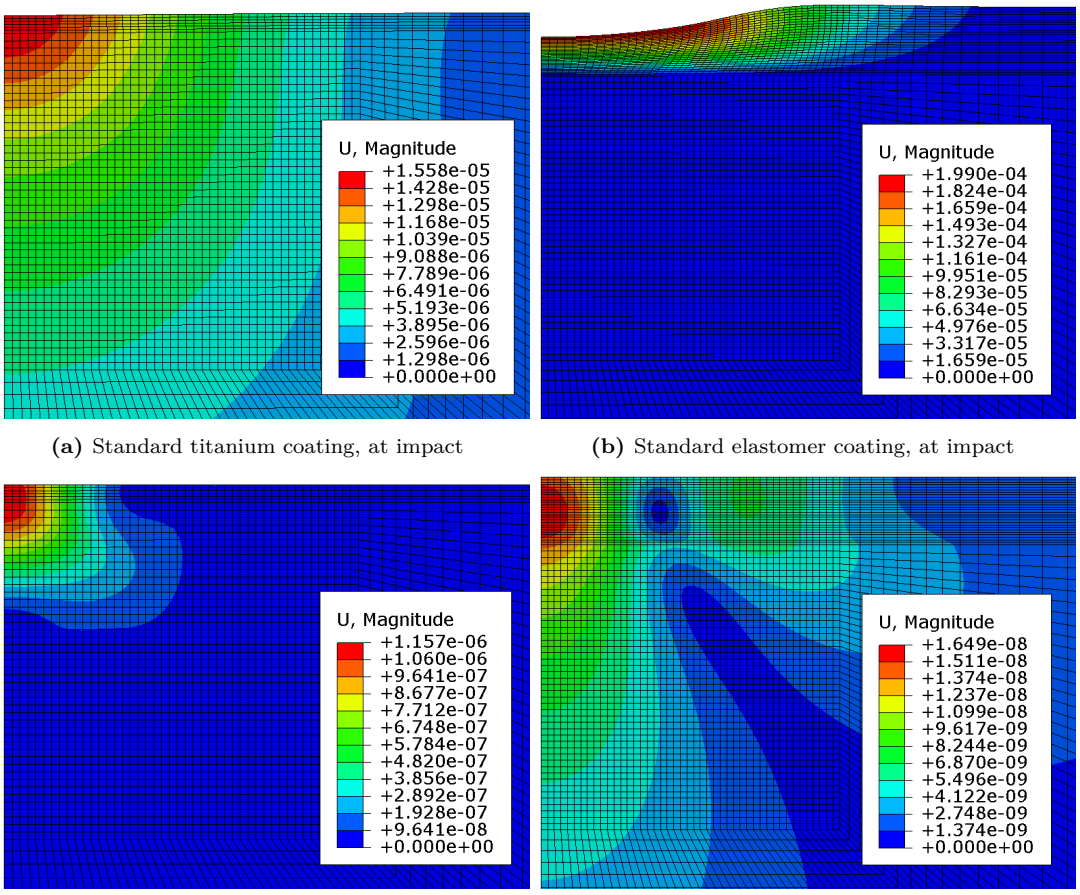

(a) Standard titanium coating, at impact

(b) Standard elastomer coating, at impact

(c) Standard titanium coating, after impact

(d) Standard elastomer coating, after impact

Figure 5.8: Displacements (in meters) at impact and after impact on an Aluminium 2024-T3 substrate

When we look at the displacements created by the droplet (Fig. 5.8), we can also observe two different behaviours, both at impact and after the impact. Even though the elastomer coating shows a higher displacement while the surface is loaded, its hyperelastic behaviour allows it to recover the elastic strains entirely when the surface is unloaded. The titanium coating is more resistant at impact but due to its plastic behaviour, the plastic strains in the coating remain after the unloading while there are none in the perfectly hyperelastic elastomer. When unloaded, the displacement in the substrate is also greater when the titanium coating is applied.

Another interesting way to look at the stress distribution is to make a cross-section view along the depth of the sample. Fig 5.9 shows the distribution of the maximum principal stress as a function of the depth along the impact axis. Graphs show the distribution for the standard titanium (a) and elastomer coating (b) on an aluminium substrate during and after impacts.

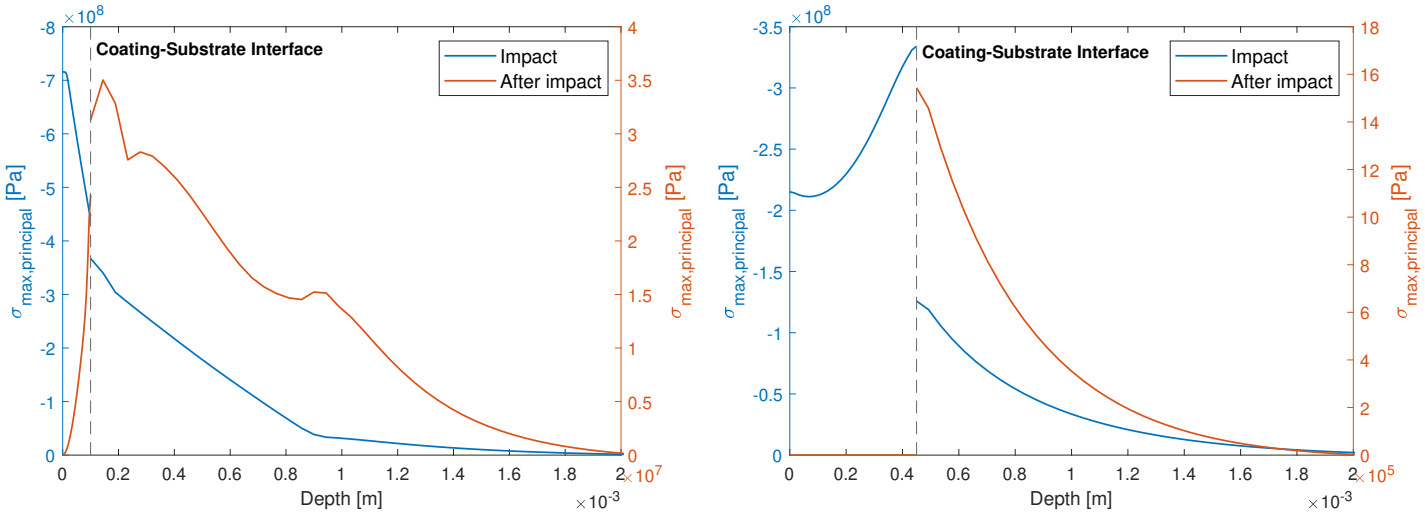

(a) Standard titanium coating

(b) Standard elastomer coating

Figure 5.9: Maximum principal stress distribution along the sample depth under the impact (0,y)

For the titanium coating (a) The stress at impact is maximum in compression at the impact point. It then keeps decreasing when looking deeper in the sample. After the unloading, the maximum principal stresses are in traction and increase from 0 MPa at the surface to around 25 MPa at the coating-substrate interface. In the substrate, they globally decrease (with three peaks) and reach a maximum of 35 MPa.

For the elastomer coating (b) During the impact the maximum principal stress is at the interface (on the coating side). Starting from surface until this maximum point, the stresses decrease shortly (up to $y = 100\mu m$) before increasing till the interface. The

interface stress gap is larger than for the titanium coating and in the aluminium substrate, the stress decreases exponentially to zero. When it is fully unloaded, the hyperelastic elastomer shows no residual stress and the distribution in the substrate is the same as during the impact only with a maximum value around 1.4 MPa.

5.3.1 Cyclic loading

As mentioned above, a simulation is constituted of cycles of loading and unloading of the top surface. On Fig. 5.10, the evolution of the maximum stress and maximum total strain (plastic and elastic) during the different cycles are shown. The values are measured at the point in the substrate who suffers the biggest plastic deformation. These values are obtained for a reference $100\mu m$ titanium coating on an aluminium substrate. When the first droplet hits the surface, the stress exceeds the yield stress of the substrate. The strain has thus an elastic and a plastic component.

When the load is removed, the elastic component of the strain disappears and only the plastic strain remains. When a new droplet hits the surface, the loading curve follows the curve of the previous unloading until the previous maximum stress is reached. Then it follows the typical stress-strain curve of aluminium until it reaches the new value of the maximum stress and the plastic strain component increases according to the stress increase. This is a typical elastic-plastic behaviour.

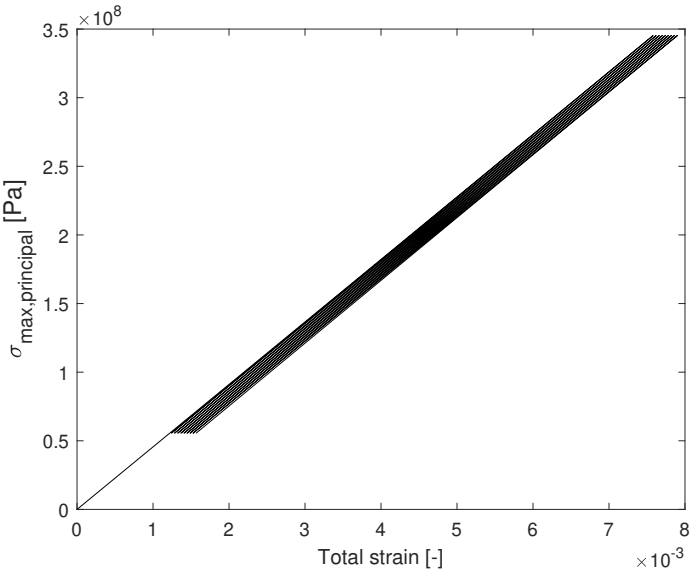

Figure 5.10: Stress-strain curve of the cyclic loading

When looking closer at the top part of the stress-strain curve, the increase of stress and plastic strain for each impact can be observed more clearly, see Fig. 5.11. The stress

increase per droplet is in our case equal to 18 kPa, which represents 0.0052 % of the initial stress (at the first droplet). This value becomes significant if you consider that the leading edge is hit by thousands of droplet over its lifetime.

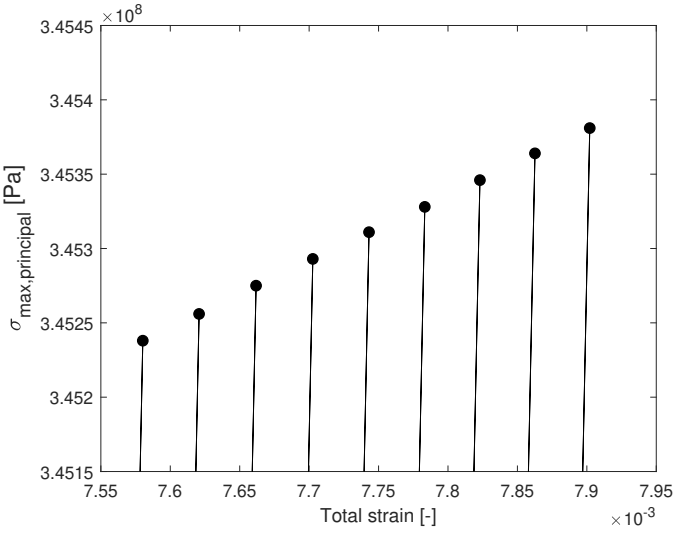

Figure 5.11: Focus on the top-side values of the stress-strain curve

5.3.2 Impact on different substrates

Our first results were obtained for different coatings on an aluminium substrate. Composite materials substrates such as our CFRP modelled previously are also frequently found in water droplet erosion applications. Fig. 5.12 shows results for the standard titanium coating conditions with both substrates.

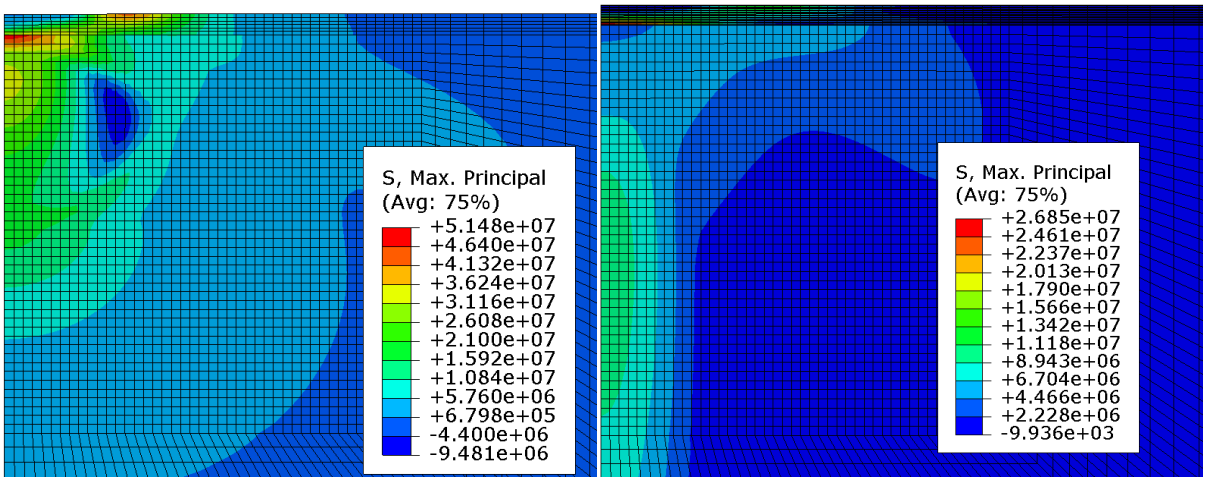

(a) Standard titanium coating on aluminium substrate **(b)** Standard titanium coating on CFRP substrate

Figure 5.12: Maximum principal stresses [Pa] after impact for titanium coating on different substrates

For the titanium coating, the response at impact is similar when applied on an aluminium or a CFRP substrate. As shown on Fig 5.13, the stress distribution at impact is the same up to a multiplying factor. A difference appeared in the distribution of the maximum principal stresses after the impacts. The zone of compression that appeared in the aluminium substrate, did not in the CFRP substrate (see Fig. 5.12). Moreover the maximum principal stress observed in the substrate is just under the interface for the aluminium substrate while it is situated deeper in the CFRP substrate. The absolute values of stresses in the coatings are also different but their comparison is made difficult because of the non-implementation of a plastic behaviour for the CFRP.

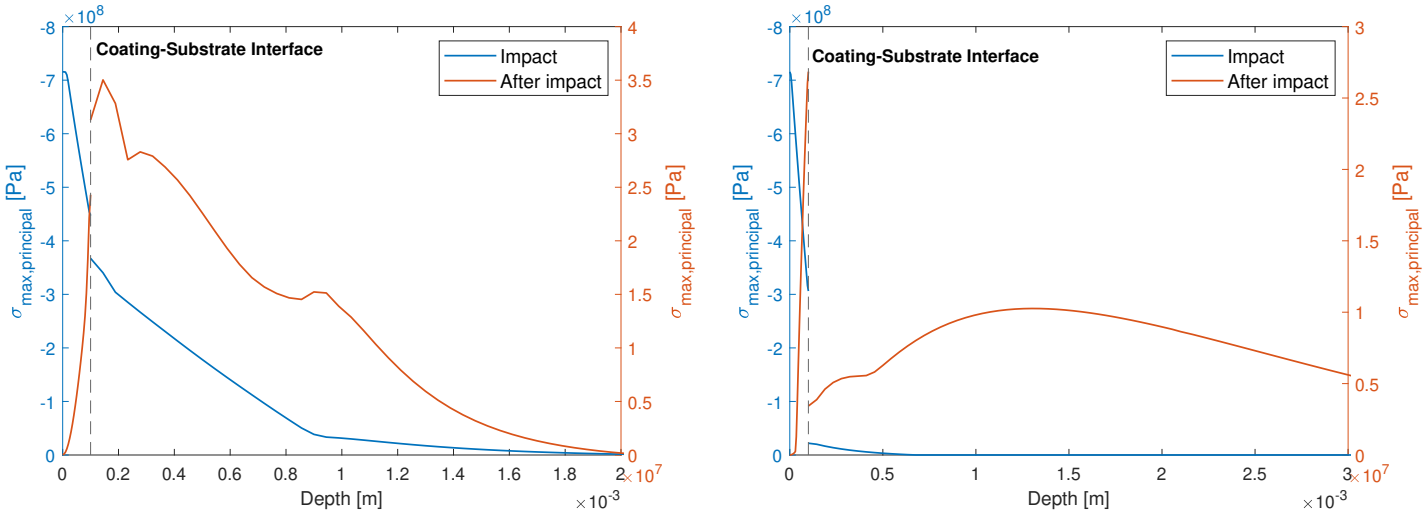

(a) Standard titanium coating on aluminium substrate

(b) Standard titanium coating on CFRP substrate

Figure 5.13: Maximum principal stresses [Pa] after impact for titanium coating on different substrates

For the elastomer coating, the stress response is different during and after the impact as shown on Fig 5.14. During the impact, the only qualitative difference is the sign inversion of the stresses in the CFRP substrate compared to the aluminium substrate. This must be caused by the fully elastic behavior of the CFRP. For the observation after impact, a major difference appears. While the stresses only appeared in the substrate on Fig. 5.14a with a big discontinuity at the interface, some small stresses appear in the elastomer coating when applied on a CFRP coating (Fig. 5.14b). Furthermore, the stress distribution is continuous at the interface and reaches a maximum deeper in the substrate.

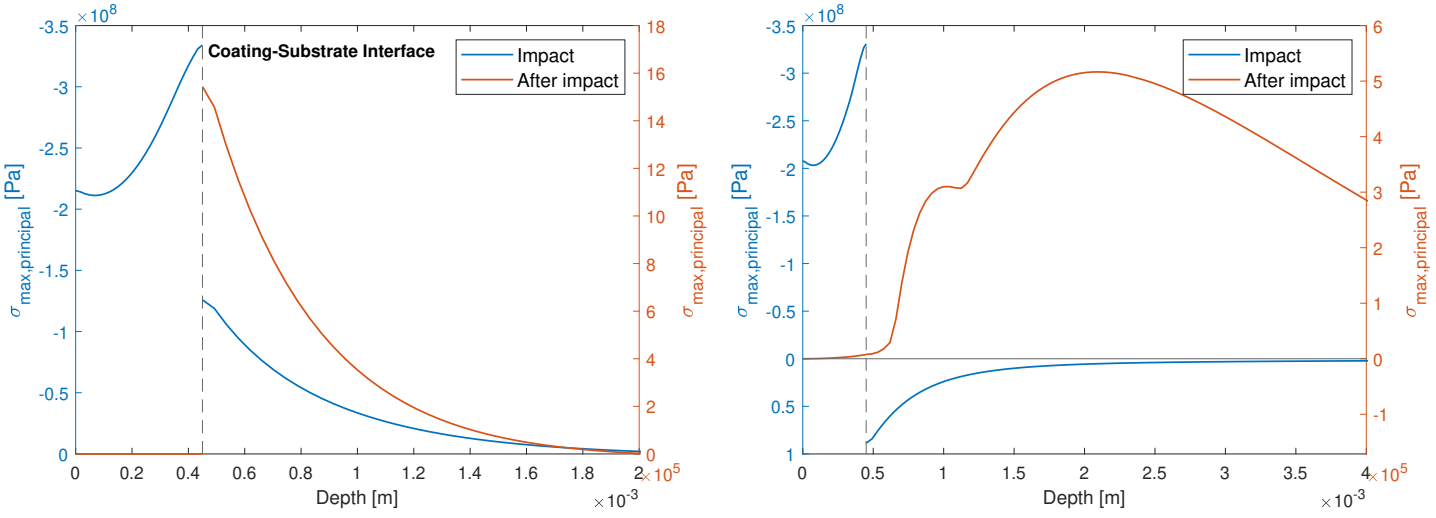

(a) Standard elastomer coating on aluminium substrate

(b) Standard elastomer coating on CFRP substrate

Figure 5.14: Maximum principal stresses [Pa] after impact for elastomer coating on different substrates

5.3.3 Influence of the thickness of the coating

When analysing the evolution of our experiments for different thicknesses, different outputs were compared depending on the type of coating. Indeed, as explained in the state of the art, the main damage mechanism will be different for our two types of coatings.

As the standard thicknesses for metallic and elastomeric coatings are respectively around 100 μm and 400 μm, we non-dimensionalised any result X with the value X_0 obtained for the corresponding reference thickness ($100\mu m$ or $400\mu m$):

$$\frac{X}{X_0} = f\left(\frac{t}{t_0}\right) \ . \tag{5.8}$$

Metallic coating

For the metallic coatings (harder and more rigid materials), surface degradation is the main damage mechanism. Therefore we analysed the evolution of the depth of the crater created by the droplets after their impact, U_0 being the crater depth using the $100\mu m$ Ni-PED21 coating.

The Ni-Bulk crater increases significantly with the thickness. This is due to its lower yield stress and ultimate stress. The more Ni-Bulk, the more parts will reach plastic deformation. The Ni-PED195 has similar values of similar values of yield stress (334 MPa vs 345 MPa for the aluminium) and ultimate stress (512 MPa vs 483 MPa). Therefore the influence of the coating on the crater size is small.

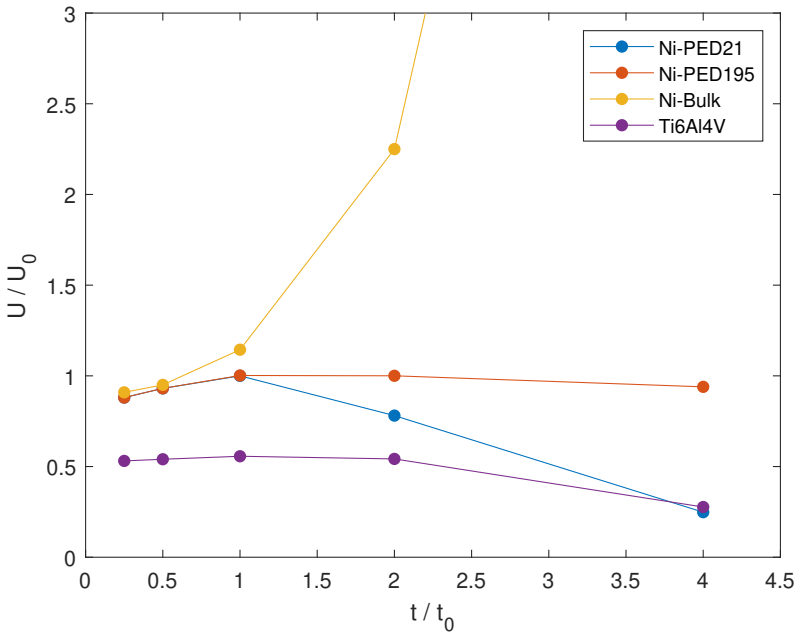

Figure 5.15: Depth of the crater after the impacts on the metallic coatings as a function of the thickness of the coating, non-dimensional

The Ni-PED21 on the other hand, has greater yield and ultimate stress. Its yield strength being above the impact load, the more Ni-PED21 coating, the less plasticity will be induced reducing the crater size.

Finally the titanium alloy already produces smaller craters for smaller thicknesses due to its different reaction to water droplet impacts. The water-hammer pressure being linked to the density and the speed of sound of the impacted material, it is lower for the titanium than for the nickel samples. The crater sizes then decreases for thicker coatings but not as fast as for the Ni-PED21. It is most certainly due to the higher mechanical properties of the Ni-PED21.

Elastomeric coating

For the elastomer coating on the other hand, the main damage mechanism is the delamination occurring at the interface between the coating and the substrate. The evolution for different coating thicknesses of the maximum shear stress at the interface during the impact, which is know to be mainly responsible for delamination [75], is represented on Fig. 5.16a.

Another interesting output is the maximum principal stress in the substrate at impact time. Indeed if delamination is avoided, the goal of the elastomer is to minimise the stress transmitted to the substrate.

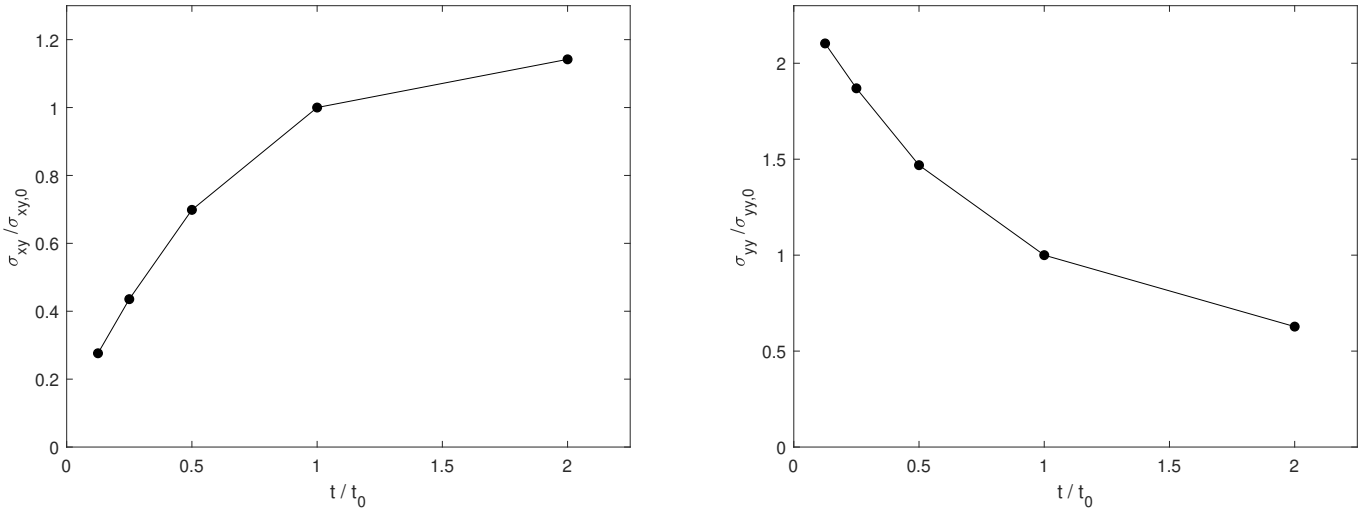

(a) Maximum shear stress at the coating-substrate interface as a function of the thickness of the coating, non-dimensional

(b) Maximum principal stress in the substrate as a function of the thickness of the coating, non-dimensional

Figure 5.16: Thickness variation with elastomeric coating

Fig. 5.16a shows that the maximum shear stress increases logarithmically with the thickness. One the other hand, the stress transmitted to the substrate has a negative logarithm form as a function of the thickness, see Fig. 5.16b.

5.3.4 Influence of impact velocity

Erosion is known to be significantly dependant on the impact velocity of the droplet, V. As described in the state of the art, the erosion rate is proportional to V^n, where the power index n varies from 2 to 7 depending on the experimental conditions. In the following section,the influence of the impact velocity on the parameters will be observed, implemented as a variation of the water-hammer pressure in the model, on the parameters mentioned before.

As done for the thickness variations, we non-dimensionalised around the reference speed of 180 m/s. We non-dimensionnalised any result X with the value X_0 obtained for the tests at the reference speed V_0:

$$\frac{X}{X_0} = f\left(\frac{V}{V_0}\right) \ . \tag{5.9}$$

The parameters analysed remain the same, based on the most significant damage observed in the literature for the different types of coatings.

Metallic coatings

The evolution of the crater depth as a function of the impact velocity is represented in Fig. 5.17, U_0 being the crater depth of the $180m/s$ droplet on the Ni-PED21 coating. The evolution follows a power-law . All the coatings follow this curve and the power index linking the crater depth and the impact velocity varies from 8.3 to 8.5 depending on the material with an average value of 8.38 :

$$\frac{U}{U_0} = k\left(\frac{v}{v_0}\right)^{8.38} \quad . \tag{5.10}$$

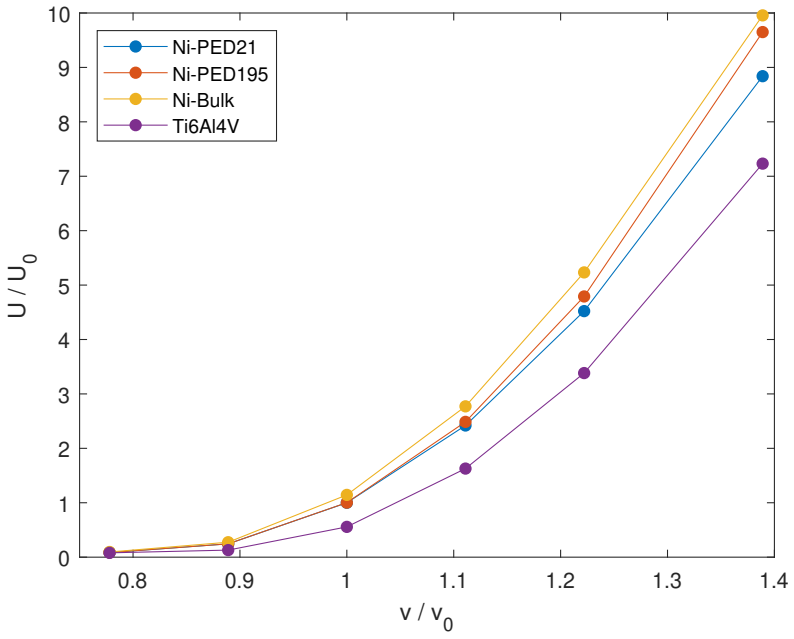

Figure 5.17: Depth of the crater after the impacts on metallic coatings as a function of droplet impact velocity, non-dimensional

Elastomeric coatings

For elastomeric coatings, both the maximum interface shear stress at impact (Fig. 5.18a) and the maximum principal stress in the substrate at impact (Fig. 5.18b) vary linearly with the impact speed of the droplets. By performing a linear regression, we obtained the slope of both graphs: 0.98 for the shear stress and 1.41 for the principal stress :

$$\frac{\sigma_{xy}}{\sigma_{xy,0}} = 0.98\left(\frac{v}{v_0}\right) \quad , \tag{5.11}$$

$$\frac{\sigma_{yy}}{\sigma_{yy,0}} = 1.41\left(\frac{v}{v_0}\right) \quad . \tag{5.12}$$

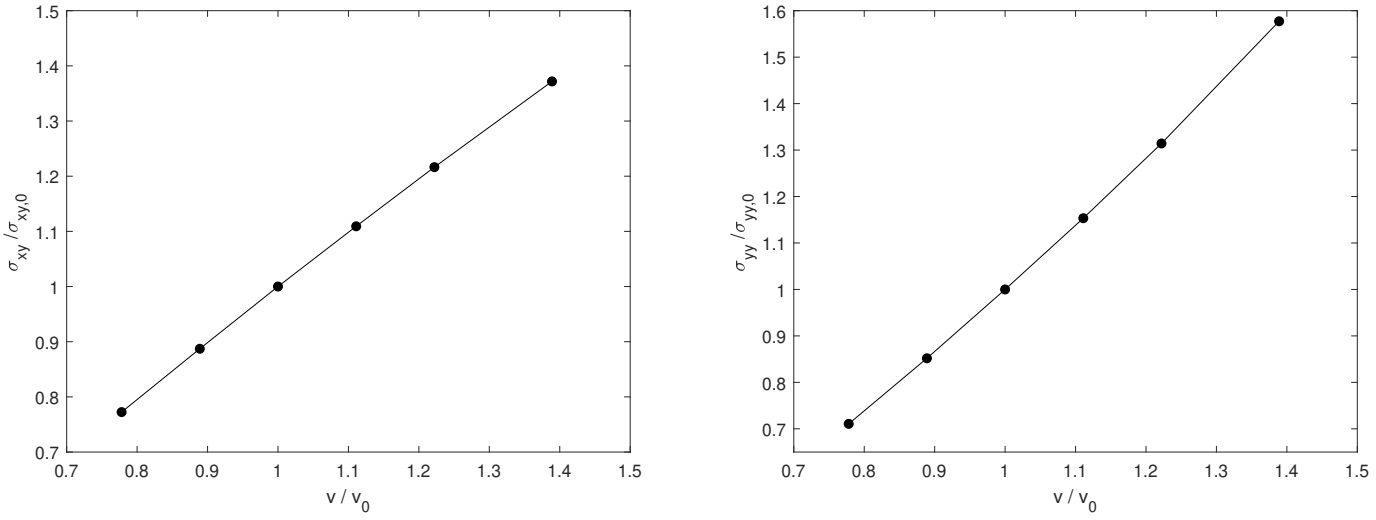

(a) Maximum shear stress at coating/substrate interface as a function of droplet impact velocity, non-dimensional

(b) Maximum principal stress in substrate as a function of droplet impact velocity, non-dimensional

Figure 5.18: Impact speed variation on elastomeric coating

5.3.5 Discussion

Considering the results obtained in the previous sections, some conclusions can be drawn on the erosion resistance of the different coatings studied :

- The tests made with the reference values based on typical usages show the main differences between a metallic and an elastomeric coating. After the impacts, metallic coatings present more damage on the impacted surface and transmit larger stresses to the substrate. Elastomer coatings absorb the impact better but show higher stresses at the coating-substrate interface, increasing the risk of debonding.

- The cyclic loading results shows that every successive droplet impact generates an additional stress, resulting in an additional strain in the target material.

- When running the reference tests but with another class of substrate, here a CFRP composite, the stress distribution is widely different after the impact. The values are lower in the CFRP substrate than in the aluminium substrate and the maximum stress value without taking the coating into account are much deeper in the CFRP substrate. During the impact, apart from some scale differences, the major difference is the substrate reaction under an elastomer coating. Starting from the interface, while the aluminium substrate presents decreasing compressional stress, the CFRP shows a decreasing tensile stress.

- The size of crater created after unloading on metallic coatings depends on its thick-

ness. But depending on the mechanical properties of the metal, the evolution will differ. When the coating thickness increases, metals that have a higher (*resp.* lower) yield stress than the substrate show a decrease (*resp.* increase) of the crater size. Moreover, the crater size also depends on the material density and speed of sound. Indeed greater values of these two parameters increase the water-hammer pressure applied to the impacted surface.

- The thickness of the coating also has an influence for elastomeric coatings. Increasing the thickness lowers the stress impacting the substrate, which is the objective for this type of coating. On the other hand, the increase of thickness is responsible for the increase of shear stress at the coating-substrate interface. This leads to possible delamination, which is the main damage mechanism for elastomeric coatings. In addition, the elastomer coated samples shows higher deformations at impact but lower deformations after the unloading.

- The impact velocity was known to be significant for the erosion rate. This study shows that the relation between the surface crater depth at the impact point and the impact velocity is also a power-law. For the tests with metallic coatings on an aluminium substrate, the exponent found has an average value of $n = 8.38$. From this we can conclude that care must be taken for high impact velocity droplet, even with high strength coatings.

- For the elastomeric coatings, the relations between the impact velocity and the stresses (shear at the interface and maximum principal in the substrate) have linear behaviour (Fig. 5.18). The stress transmitted to the substrate increases faster that the shear stress at the interface, thus high velocity impact will be more likely to cause damage in the substrate than causing coating-substrate delamination.

Conclusion

Today, the importance of the energy management increases day after day and no inversion of that trend seems to be around the corner. Therefore the interest for the erosion issue in aerospace and windmill applications is rising very fast because of the benefits it could lead to.

Throughout the first part of this work, the goal was to bring a global understanding of the water droplet erosion of leading edges issue. Therefore we started by describing the whole water droplet erosion mechanisms, the liquid-solid impact first and the solid damage mechanisms then. Afterwards, three materials parameters impacting the erosion rate and often discusses in the literature were presented: hardness, impedance and roughness. The quantitative study lead into the second part did not discussed all of them but added some more. In the last chapter of the state of the art we tried to classify the existing protection solutions: coatings, leading edge tapes and erosion shields. The major advantages and disadvantages of each solution were presented and discussed. The effects on erosion for each solution are different but so do the defects and their appearance rate, the adhesion between each solution and its substrate, and the aerodynamic losses.

The second part presents the water droplet erosion tests we conducted. First we described the test bench developed at UCLouvain that was supposed to be used for all this second part. Unfortunately, due to the health situation and the measures taken by the UCLouvain, we had to review our plans. It was decided to switch from experimental tests to a numerical analysis on *Abaqus*. With the time available and our basic knowledge of the program, we limited ourselves to the modeling of the first damage mechanism of erosion, direct deformation. Indeed by delaying direct deformation, the impact of the other mechanisms will decrease.

All the elements of the numerical model were then fully described: the finite element model, the liquid-solid impact, the cyclic loading and finally the material properties and constitutive models. Then the limits of the model were discussed to be able to draw adapted conclusions. We implemented different coating materials (Ti6Al4V, different deposited Nickels and an elastomer model) and different substrate (Aluminium 2024-T3 and a CFRP composite). Tests were then performed with different parameters combinations of coating material, substrate material, coating thickness and droplet velocity.

The tests conducted allowed us to confirm some of the conclusions already stated in the first part, such as the determination of the main mechanism of erosion of metallic and elastomeric coatings, and to make some others. The variations and behaviors of the erosion reactions were then analysed for all the parameters studied. In a final discussion we tried to explain the different behaviors observed.

However, erosion is such a complex mechanism that only the influence, for the first damage mechanism, of parts of the parameters were analysed during this work. Further experiments should be conducted in the near future on the test bench of UCLouvain or by further developing the numerical model. Further research should focus on the implementation of failure mechanisms. The appearance of a non-perfect surface roughness would also allow to implement two other erosion mechanisms : lateral outflow and hydraulic penetration.

Appendices

Appendix A : Test bench procedure (French)

24/02/2019

PILOTE D'EROSION AUX GOUTTES D'EAU
(Réaumur, étage -1)

Procédure d'utilisation pour le pilote d'érosion aux gouttes d'eau

P Bollen

L. Wautier

CONSIGNES EN CAS DE PROBLÈME SUR CETTE INSTALLATION

N° de téléphones

1. **Luc Wautier 010 / 47 23 35**
2. **Pierre Bollen 010 / 472338**
3. **Secrétariat 010 / 47 24 87**

Si problème ?

1. **Technique bâtiment : maintenance UCL 010 / 47 89 89**
2. **Sécurité : Mme Wathelet 010 / 47 87 33**
   Mme Wilbaut 010 / 47 87 32 secrétariat 010 / 47 87 31
3. **Le numéro de la permanence UCL est 010 / 47 24 24**

URGENCE : 010 / 47 22 22

Vous êtes dans le **bâtiment Réaumur Hall E, étage 0 , voie Minckelers 1,** (institut iMMC pôle IMAP)

Le numéro de téléphone du local est le **010 / 47 23 37**

Entre postes téléphoniques UCL, uniquement les 5 derniers chiffres sont à composer

0. Principe de fonctionnement de l'installation.

Le but de l'installation est de mesurer la résistance d'un matériau à l'érosion par l'impact de gouttes d'eau à haute vitesse. Le fonctionnement est le suivant, un moteur fait tourner un bras au bout duquel se trouve l'échantillon. Tout au long du parcours de l'échantillon, des aiguilles laissent tomber en continu des gouttes, lesquelles sont frappées par l'échantillon.

1. Avant de travailler avec la machine

0. Chaque intervention sur l'installation doit être registrée dans le cahier de la machine.
1. **Toujours déconnecter l'alimentation de courant avant de travailler sur l'installation (figure 7).**
2. La protection individuelle est obligatoire. Elle consiste de chaussures et lunettes de sécurité et un casque anti-bruit.



3. Assurez-vous que l'emplacement autour de l'installation soit bien rangé à fin de pouvoir facilement circuler autour.

2. Echantillons

0. Les échantillons sont usinés comme des cylindres de 30 mm de diamètre et d'épaisseur variable.

Remarque: La détection d'endommagement en surface peut parfois être difficile. Referez-vous aux méthodes de polissage si nécessaire.

Avant chaque test, les conditions de surface initiales doivent être inspectées par microscope et le poids initial de l'échantillon est enregistré.

1. Les échantillons sont fixés en commençant par dévisser l'anneau de serrage.(figure 2)
2. Placez l'échantillon contre la plaque en enfonçant le ressort. (figure 3)
3. Revissez l'anneau de serrage pour maintenir l'échantillon en place.
4. Suivez les instructions pour démarrer le test dans le chapitre suivant.
5. Veiller à limiter l'accès aux seules personnes autorisées (barrière avec signalisation à placer)
6. Après l'essai, retirer l'échantillon du support.
7. Nettoyez l'échantillon à l'**acétone** (si le matériau le permet) et séchez-le

Port de lunettes de sécurité obligatoire. 

ATTENTION : MANIPULATION SOUS HOTTE OBLIGATOIRE- lire la FDS en annexe
Mentions de danger :
H225 Liquide et vapeurs très inflammables.
H319 Provoque une sévère irritation des yeux.
H336 Peut provoquer somnolence ou vertige

8. Examinez la surface au microscope (électronique) et enregistrez le poids final.

Figure 2: Anneau vissé

Figure 3 : Anneau dévissé + Plaque avec ressort

Remarque: les variations de masse avant-après essais peuvent être très petites pour certains matériaux/conditions d'essai. Il faut être spécialement attentif de bien sécher l'échantillon avant de le peser. Prenez également en compte que certains matériaux gagnent en masse à cause de l'absorption d'humidité.

3. Câblage électrique de l'installation

Le diagramme de câblage est expliqué ci-dessous. 3x380V alimente la boite de contrôle. Le circuit peut être coupé par deux boutons d'arrêt d'urgence (figure 5), deux interrupteurs de contact 'normalement ouvert' (figure 7), le détecteur de fumée ou un bouton « STOP ».

Le variateur de fréquence ne peut qu'être activé si tous les interrupteurs sont fermés, le bouton « START » est déclenché et que le switch du variateur de fréquence est placé sur « 1 ». En revanche, le variateur s'éteint si un ou plusieurs boutons d'arrêt sont déclenchés.

La vitesse de rotation du moteur est ajustée par le variateur de fréquence sous l'effet d'un potentiomètre placé sur le boitier principal.

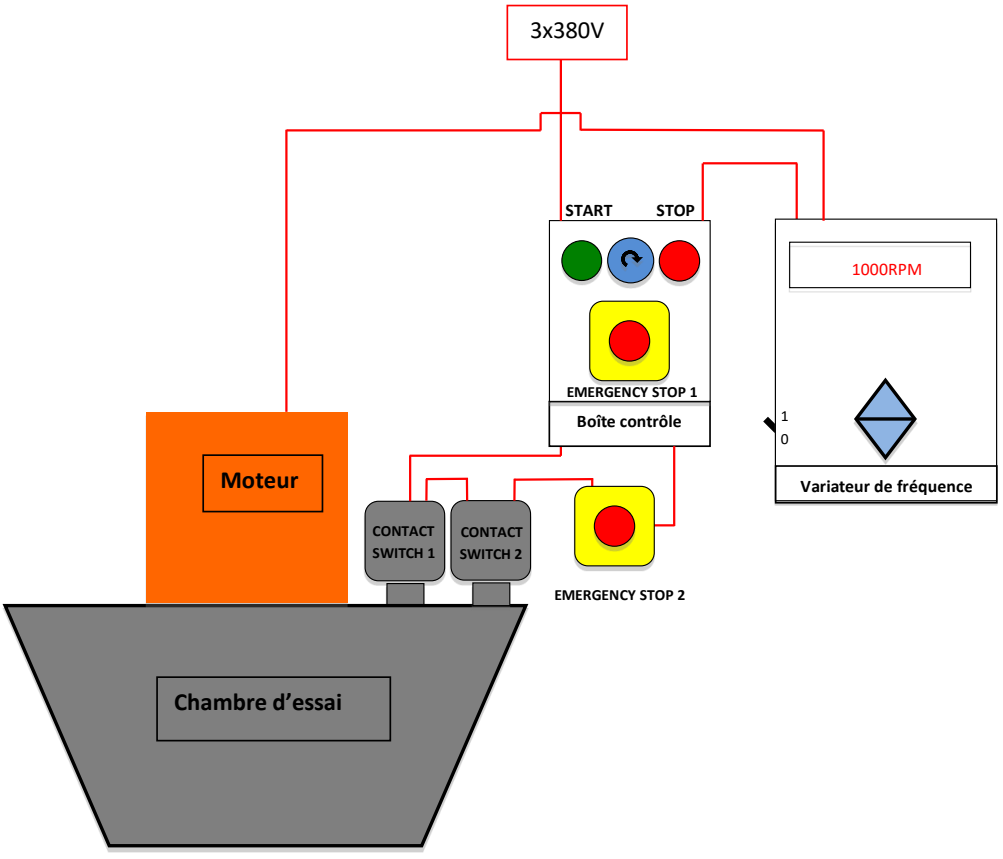

Figure 1 : Câblage électrique du pilote

(a) (b)

Figure 5 (a) Le boitier principal avec les boutons START/STOP et un bouton d'arrêt d'urgence (b) Le bouton d'arrêt d'urgence à l'extérieur de la salle

(a) (b) (c)

Figure 6: les différentes prises électriques: a) 3x380V vers moteur et alimentation générale b) 3x380V vers boîte de contrôle c) contrôle vers interrupteurs de contact et détecteur de fumée. Toutes ces prises doivent être débranchées comme sécurité supplémentaire quand l'équipement n'est pas utilisé

(a) (b)

Figure 7 : Deux interrupteurs de contact. (a) Porte extérieure (b) Porte intérieure

4. Production de gouttes

Les conditions opératoires de base (référence Sonaca) pour la production de gouttes sont:

Intensité de pluie: 20mm/h
Taille de la goutte: Ø 2mm

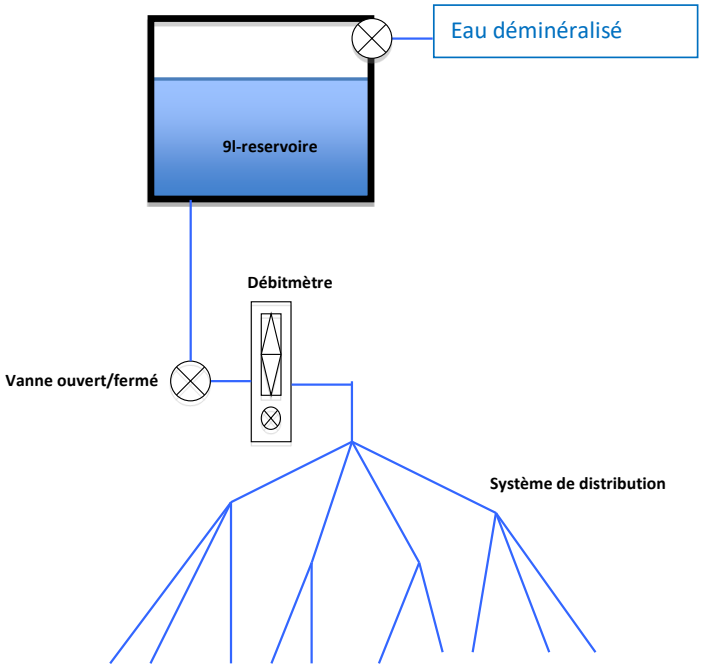

Figure 8 : Système de distribution de pression

La système de distribution présenté ci-dessus est raccordé à l'eau de ville (fig. 10a), l'eau s'écoule dans la canalisation et passe dans le système de filtration avant d'être envoyée dans le débitmètre (fig. 10b) puis répartie dans les tuyaux de distribution (fig. 9b) afin d'être dirigée vers les différentes aiguilles pour former des gouttes.

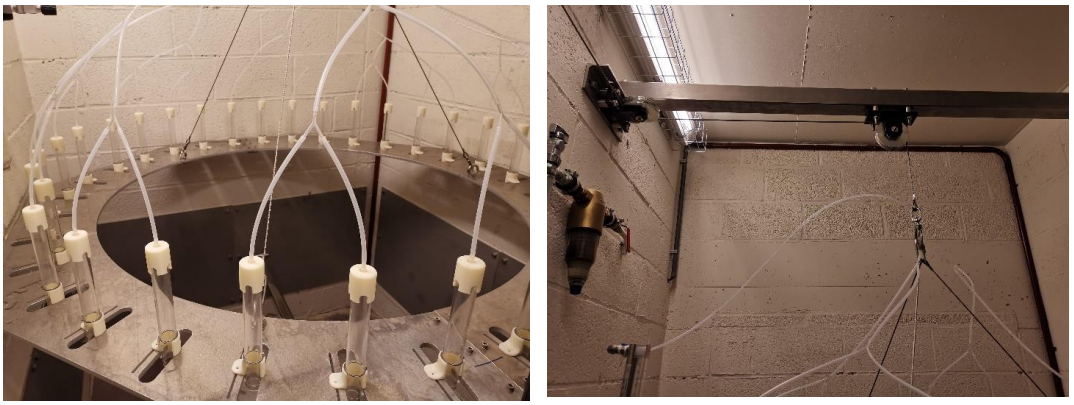

(a) (b)

Figure 9 : (a) Anneau avec pipettes d'eau (b) Raccordement débitmètre-anneau

Figure 10: (a)Vanne (fermée) *(b) Débitmètre*

32 aiguilles (orifice 30G) sont utilisées pour produire les gouttes de dimensions adéquates. Les aiguilles sont percées à travers de bouchons en plastique et placé dans des tubes à essais pour accélérer les gouttes verticalement dans une zone sans turbulences avant d'entrer la chambre d'essai (figure 11).

Figure 11: Setup des points d'injection

Water injection		
Intensité de pluie	20,00	mm/h
R1 (rayon intérieure)	0,771	m
R2 (rayon extérieure	0,799	m
A(surface échantillon)	6.1575	cm^2
Volume/h	1,21E-03	m^3/h
Volume/h	1,21	l/h
# aiguilles	32,00	
Diamètre de goutte	2,00	mm
Volume de gouttes	4,19E-09	m^3
Gouttes/h	288750,00	drops/h
Gouttes/sec	80,21	drops/second
Gouttes/(aiguille*sec)	2,51	Drops/(aiguille*sec)

Table 1 : Calcule du débit et des nombre d'aiguilles nécessaires

Avant l'essai, l'intensité de pluie devrait être calibrée en ouvrant la vanne et prenant la mesure sur le débitmètre. La quantité peut être ajustée à l'aide de ce débitmètre

Remarque 1: Il existe une erreur dans la calibration provenant de la présence d'une petite quantité d'eau sur paroi de la chambre.

Remarque 2: Pendant l'essai, de petites fluctuations de débit sont possibles. Celles-ci sont moyennées sur une durée d'essai longue.

Remarque 3: Bien que le débitmètre soit conçu pour travailler entre 0,5 et 5l/h, le débit maximal est d'environ 3l/h. Ceci est dû à la grande perte de charge des orifices des aiguilles.

Remarque 4: Soyez prudent parce qu'un point d'injection peut produire un flux anormal (plus élevé ou plus faible que les autres points) ou produire des gouttes qui touchent les parois des tubes à essai avant d'entrer dans la chambre. Essayez de remplacer l'aiguille ou d'ajuster le bouchon en plastique.

5. Activation du pilote

1. Positionner les boutons d'arrêt d'urgence sur off (intérieur et exterieur)
2. Assurez-vous que l'échantillon soit bien fixé

ATTENTION : RISQUE DE PROJECTION LIE A LA FORCE CENTRIFUGE DE L'INSTALLATION : PLACEMENT ET VERIFICATION DE TOUS LES SYSTEMES DE FIXATION OBLIGATOIRE !

3. Ouvrez la vanne d'arrivée d'eau (fig. 10a) et assurez-vous que tous les points d'injection produisent des gouttes adéquates
4. **Remettre la position du switch sur le côté du variateur de fréquence et le potentiomètre sur le boitier électrique à 0**.
5. Branchez la prise moteur située sous le moteur (fig. 6a)
6. Fermez la porte de sécurité intérieure et fermez le loquet au sol (fig. 13a&b)
7. Fermez la porte de sécurité extérieure et fermez le loquet sur la paroi (fig. 14a&b)
8. Branchez la prise moteur située dans le sas sous le boitier (fig. 6b)
9. Branchez la prise des interrupteurs d'urgence (fig. 6c)
10. Déverrouiller les boutons d'arrêt d'urgence (intérieur et extérieur)
11. Allumez le bouton START sur le boitier principal (fig. 5a)
12. Positionnez l'interrupteur du régulateur de vitesse sur la position 1 (fig. 5a)
13. Ajustez la vitesse de rotation aux paramètres d'essai désirés
14. Démarrez le chronomètre pour mesurer la durée de l'essai

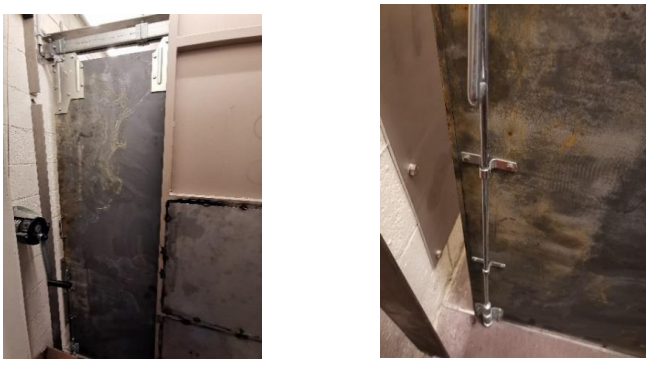

(a) *(b)*

Figure 13 : (a) Porte de sécurité intérieure (b) Loquet de la porte de sécurité intérieure

(a) *(b)*

Figure 14 : (a) Porte de sécurité extérieure (b) Loquet de la porte de sécurité extérieure

V_angulaire (RPM)	V_linéaire (m/s)	V_lineaire (km/h)
100	8.22	29.59
200	16.44	59.19
300	24.66	88.78
400	32.88	118.38
500	41.10	147.97
600	49.32	177.56
700	57.54	207.16
800	65.76	236.75
900	73.98	266.34
1000	82.21	295.94
1100	90.43	325.53
1200	98.65	355.13
1300	106.87	384.72
1400	115.09	414.31
1500	123.31	443.91
1600	131.53	473.50
1700	139.75	503.09
1800	147.97	532.69
1900	156.19	562.28
2000	164.41	591.88
2100	172.63	621.47
2200	180.85	651.06
2300	189.07	680.66
2400	197.29	710.25
2500	205.51	739.85
2600	213.73	769.44
2700	221.95	799.03
2800	230.17	828.63
2900	238.39	858.22
3000	246.62	887.81

Table 2: conversion RPM vers vitesse linéaire de l'échantillon (0,785m rayon)

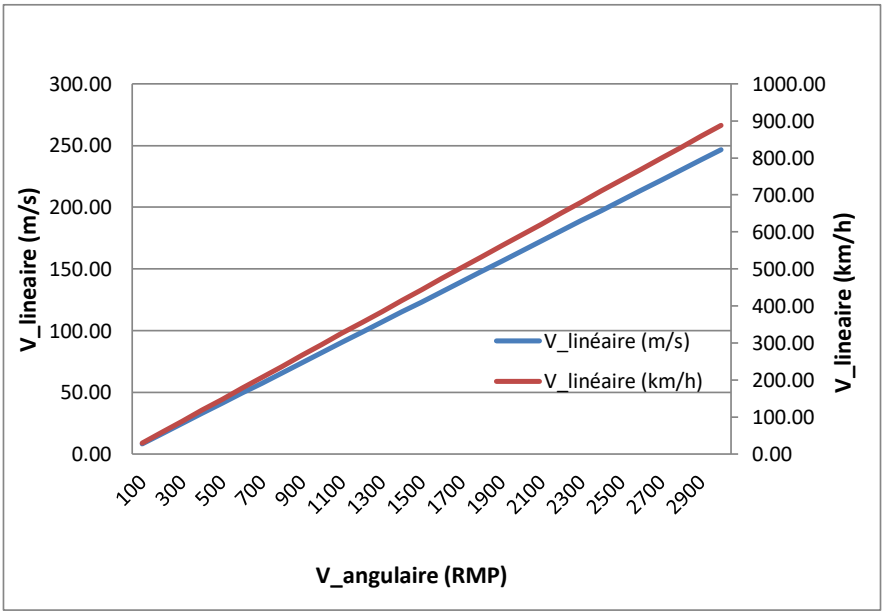

Figure 25: Variable frequency drive

Remarque 1: Une vitesse maximale de rotation de 1000RPM a été utilisée pour les premiers essais. Cette vitesse est plus basse que préconisé par Sonaca mais ne perturbe pas les gouttes.

6. Arrêt de l'essai (arrêt normal)

1. Arrêter le chronomètre
2. Réduisez **progressivement** la vitesse du variateur à 0
3. Positionnez le switch du variateur sur 0
4. Quand le rotor est arrêté, appuyez sur le bouton stop de la boite de contrôle et déclenchez également les autres boutons d'arrêt par sécurité (fig. 5a & 5b).
5. Déconnectez la prise du moteur dans le sas (fig. 6b)
6. Déconnectez la prise des switchs dans le sas (fig. 6c)
7. Levez le loquet et ouvrez la porte extérieure
8. Levez le loquet au sol et ouvrez la porte intérieure
9. Déconnectez la prise du moteur située sous le moteur (fig. 6a)
10. Fermez la vanne d'eau

7. Arrêt d'urgence (EN CAS DE DANGER!)

1. Enclenchez un des boutons d'arrêt d'urgence. (Un est situé sur le boitier de contrôle, l'autre est à l'extérieur de la pièce.)
2. Appuyez sur le bouton stop de la boite de contrôle et déclenchez également les autres boutons d'arrêt par sécurité.

ATTENTION : ARRÊT COMPLET OBLIGATOIRE PRÉALABLEMENT À L'OUVERTURE

L'installation ne peut être remise en service qu'après accord et validation sur place des responsables de l'installation : M. P. BOLLEN

8. Annexe 1: Fournisseurs

Y-connectors

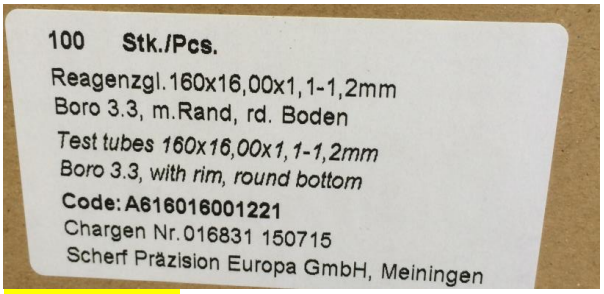

Glass tubes: VWR

Cork stoppers

Hypodermal needles

Luers connectors

9. Annexe 3 Data technique

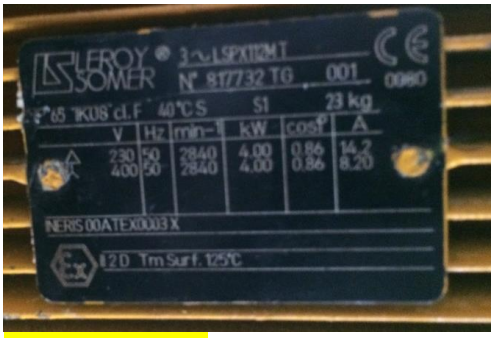

Motor specifications

Frequency Drive specifications

Attention > Bien obtenir la déclaration CE

Figure: Control Box

Break parameters in the Control Box

10. Annexe 4 Dessins techniques

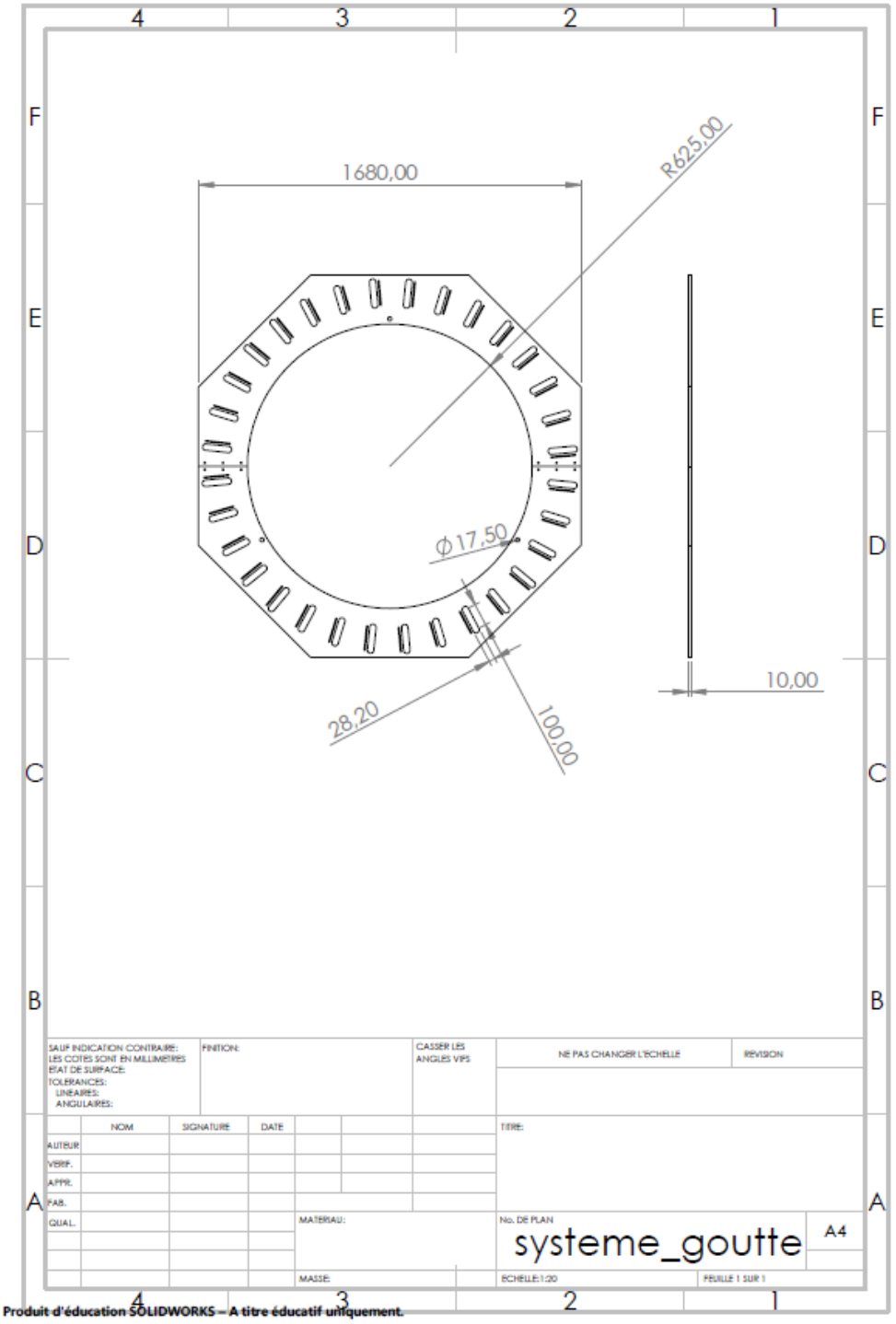

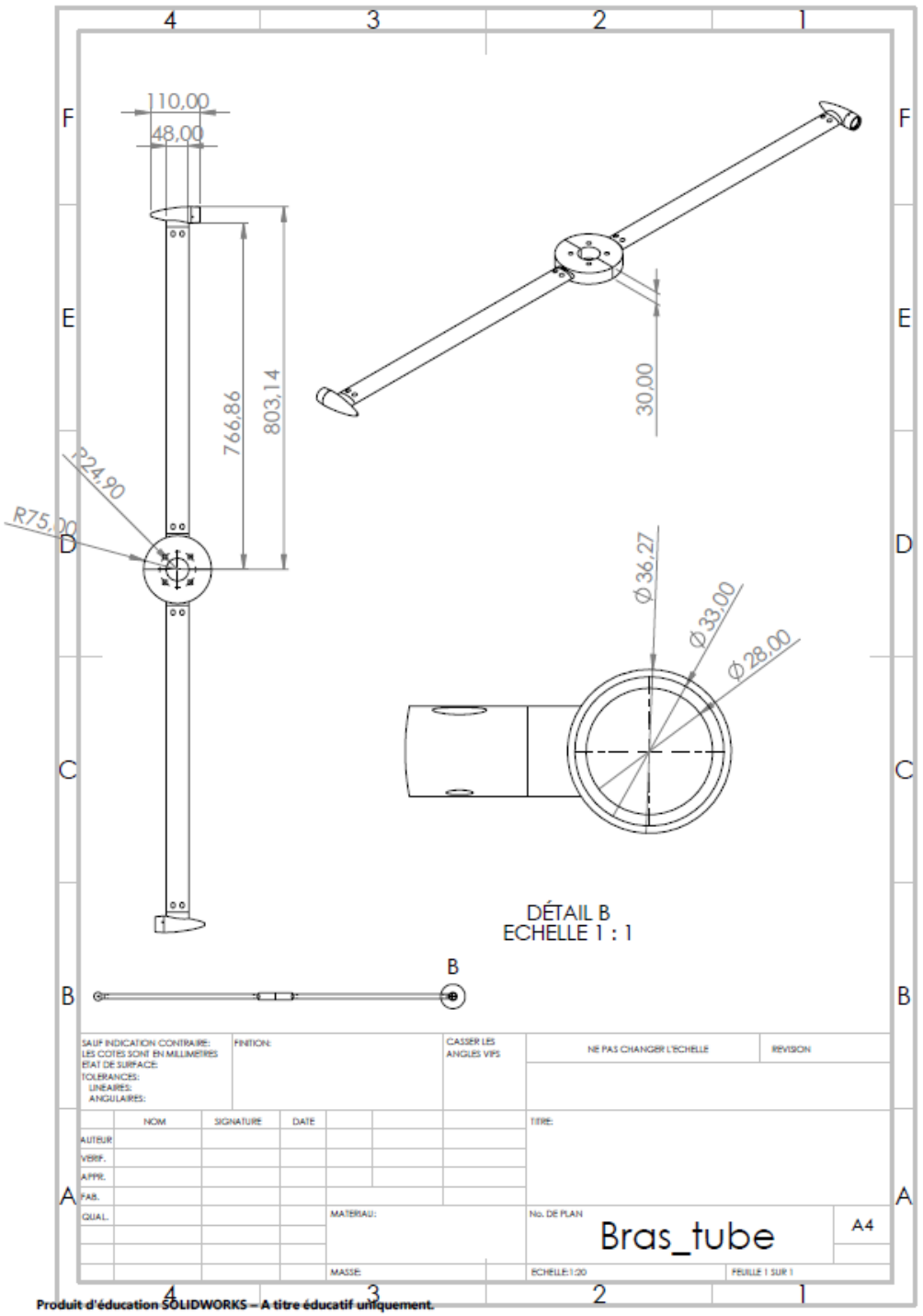
110,00
48,00
766,86
803,14
R24,90
R75,00
30,00
Ø 36,27
Ø 33,00
Ø 28,00
DÉTAIL B
ECHELLE 1 : 1
B
Bras_tube
A4
Produit d'éducation SOLIDWORKS – A titre éducatif uniquement.

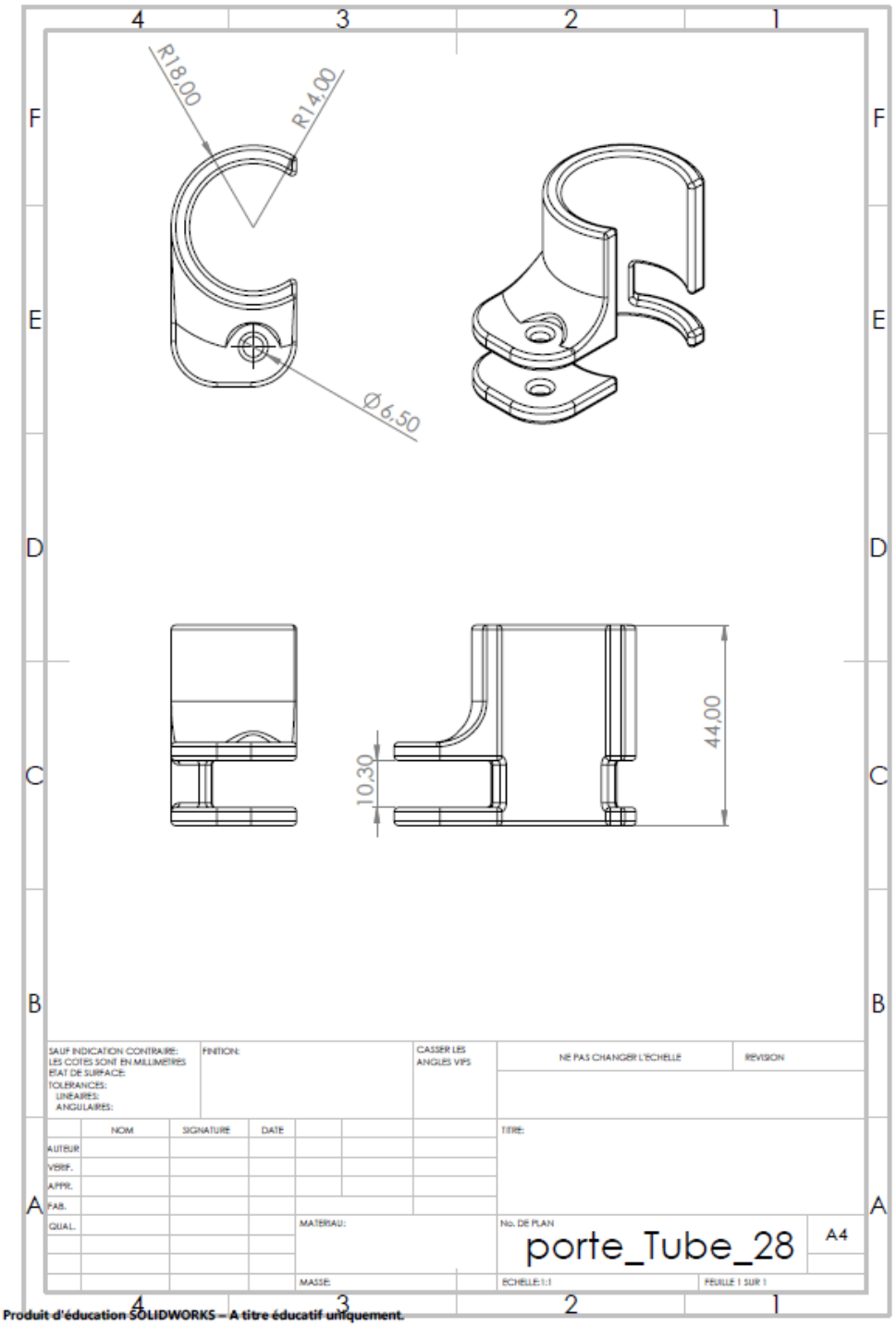
R18.00
R14.00
Ø6.50
10.30
44.00
SAUF INDICATION CONTRAIRE:
LES COTES SONT EN MILLIMETRES
ETAT DE SURFACE:
TOLERANCES:
LINEAIRES:
ANGULAIRES:
FINITION:
CASSER LES ANGLES VIFS
NE PAS CHANGER L'ECHELLE
REVISION
NOM
SIGNATURE
DATE
AUTEUR
VERIF.
APPR.
FAB.
QUAL.
TITRE:
MATERIAU:
MASSE:
No. DE PLAN
porte_Tube_28
A4
ECHELLE 1:1
FEUILLE 1 SUR 1
Produit d'éducation SOLIDWORKS – A titre éducatif uniquement.

Bibliography

[1] *Cambridge Dictionary*. URL: https://dictionary.cambridge.org/dictionary/english/erosion.

[2] C.M. Preece and N.H. Macmillan. "Erosion". In: *Annual Review of Materials Science* 7 (1977), pp. 95–121.

[3] G. Poulton. *Aviation's material evolution*. 2017. URL: https://www.airbus.com/newsroom/news/en/2017/02/Material-evolution.html.

[4] R. Herring, K. Dyer, F. Martin, and C. Ward. "The increasing importance of leading edge erosion and a review of existing protection solutions". In: *Renewable and Sustainable Energy Reviews* 115 (2019).

[5] N. Gaudern. "A practical study of the aerodynamic impact of wind turbine blade leading edge erosion". In: *Journal of Physics: Conference Series* 524 (2014).

[6] A. Sareen, C.A. Sapre, and M.S. Selig. "Effects of leading edge erosion on wind turbine blade performance". In: *Wind Energy* 17 (2013).

[7] W. Han, J. Kim, and B. Kim. "Effects of contamination and erosion at the leading edge of blade tip airfoils on the annual energy production of wind turbines". In: *Renewable Energy* 115 (2018).

[8] D.C. Maniaci, E.B. White, B. Wilcox, C.M. Langel, C.P. van Dam, and J.A. Paquette. "Experimental Measurement and CFD Model Development of Thick Wind Turbine Airfoils with Leading Edge Erosion". In: *Journal of Physics: Conference Series* 753 (2016).

[9] R. Wiser et al. "Forecasting Wind Energy Costs and Cost Drivers: The Views of the World's Leading Experts". In: (2016).

[10] J. Cresswell. "North Sea company offers radical turbine blades protection solution". In: *The Press and Journal* (2016).

[11] J. Cresswell. "Blade leading edge erosion: damage limitation, containment and prevention". In: *PES Wind Talk Point* (2018), pp. 1–3.

[12] H. GL Garrad. "A Guide to UK Offshore Wind Operations and Maintenance". In: (2013).

[13] ORE Catapult. "Develop alternative leading edge protection solutions for repairing existing blades in service". In: (2018).

[14] M.E. Ibrahim and M. Medraj. "Water Droplet Erosion of Wind Turbine Blades: Mechanics, Testing, Modeling and Future Perspectives". In: *materials* (2019).

[15] M.H. Keegan, D.H. Nash, and M.M. Stack. “On erosion issues associated with the leading edge of wind turbine blades”. In: *Journal of Physics D: Applied Physics* (2013).

[16] S.S. Cook. “Erosion by water-hammer”. In: (1928).

[17] J.P. Dear and J.E. Field. “High-speed photography of surface geometry effects in liquid/solid impact”. In: *Journal of Applied Physics* (1988).

[18] F.J. Heymann. “High speed impact between a liquid drop and a solid surface”. In: *Journal of Applied Physics* (1969).

[19] Na Li, Qulan Zhou, Xi Chen, Tongmo Xu, Shien Hui, and Di Zhang. “Liquid drop impact on solid surface with application to water drop erosionon turbine blades, Part I: Nonlinear wave model and solution ofone-dimensional impact”. In: *International Jounal of Mechanical Sciences* (2008).

[20] Jenkins and Booker. “The impingment of water drops on a surface moving at high speed”. In: *Proceedings of the Aerodynamics Capture Particles* (1960).

[21] Engel. “Waterdrop collisions with solid surfaces”. In: *Journal of Research of the National Bureau of Standards* (1955).

[22] P.A. Coulon. “Erosion-corrosion in steam turbines, Part II”. In: *Lubrication engineering* (1986).

[23] F.J. Heymann. “A survey of clues to the relation between erosion rate and impact parameters”. In: *2nd International Conference of Rain Erosion and Allied Phenomena* (1967).

[24] Eisenberg, Laustsen, and Stege. “Wind turbine blade coating leading edge rain erosion model”. In: *Wind energy* (2018).

[25] Lee, Riu, Shin, and Kwon. “Development of a water droplet erosion model for large steam turbine blades”. In: *KSME International journal* (2003).

[26] Lee, Riu, Shin, and Kwon. “Experimental assessment of droplet impact erosion of low-pressure steam turbine blades”. In: *Institut für Thermische Strömungsmaschinen und Maschinenlaboratorium der Universität Stuttgart* (2009).

[27] Hattori and Lin. “Effect of droplet diameter on liquid impingement erosion”. In: *7th International Symposium on Measurement Techniques for Multiphase Flows* (2012).

[28] J.E. Field, M.B. Lesser, and J.P. Dear. “Studies of two-dimensional liquid-wedge impact and their relevance to liquid-drop impact problems”. In: *Physical and Engineering Sciences* (1985).

[29] Mohammad Sadegh Mahdipoor. “Water droplet erosion materials and surface treatments”. PhD thesis. Montreal, Quebec, Canada: Concordia University, 2016.

[30] Na Li, Qulan Zhou, Xi Chen, Tongmo Xu, Shien Hui, and Di Zhang. “Liquid drop impact on solid surface with application to water drop erosionon turbine blades, Part II: Axisymetric solution and erosion analysis”. In: *International Jounal of Mechanical Sciences* (2008).

[31] H.S. Kirols, D.Kevorkov, A.Uihlein, and M.Medraj. "The effect of initial roughness on water droplet erosion behavior". In: *Wear* (2015).

[32] Dina Ma. "Liquid impingement erosion performance of low plasticity burnished Ti6Al4V". PhD thesis. 2014.

[33] M.S. Mahdipoor, D.Kevorkov, P. Jedrzejowski, and M. Medraj. "Water droplet erosion mechanism of nearly fully-lamellar gammaTiAl alloy". In: *Materials and Design* (2015).

[34] Nobuyuki Fujisawaa et al. "The influence of material hardness on liquid droplet impingement erosion". In: *Nuclear Engineering and Design* (2015).

[35] *Vickers hardness test*. 2020. URL: https://en.wikipedia.org/wiki/Vickers_hardness_test.

[36] Miyata and Isomoto. "Erosion phenomenon caused by water droplet impingement and life prediction of industrial materials, part 1". In: *Zairyo-to-Kankyo* 57 (2008), pp. 138–145.

[37] P.L.N. Fernando, Damith Mohotti, Alex Remennikov, P.J. Hazell, H. Wang, and Ali Amin. "Experimental numerical and analytical study on the shock wave propagation through impedance-graded multi-metallic systems". In: *International Journal of Mechanical Sciences* (2020).

[38] K. Fujisawa, M. Ohki, and N. Fujisawa. "Influence of surface roughness on liquid droplet impingement erosion". In: *Wear* 423-433 (2019).

[39] Mark Hugh Keegan, David Nash, and Margaret Stack. "Wind Turbine Blade Leading Edge Erosion : An Investigation of Rain Droplet and Hailstone Impact Induced Damage Mechanisms". PhD thesis. Glasgow: University Of Strathclyde, 2014. URL: https://strathprints.strath.ac.uk/58904/.

[40] B. Attaf. "Designing Composite Wind Turbine Blades from Cradle to Cradle". In: (2013), pp. 1–24.

[41] E. Cortes, F. Sánchez, A. O'Carroll, B. Madramany, M. Hardiman, and T.M. Young. "On the Material Characterisation of Wind Turbine Blade Coatings: The Effect of Interphase Coating–Laminate Adhesion on Rain Erosion Performance". In: *Materials* (2017).

[42] J.E. Field. "ELSI conference: invited lecture: Liquid impact: theory, experiment, applications". In: *Wear* 233-235 (1999), pp. 412-427 02–031.

[43] H.M Slot, E.R.M. Gelinck, C. Rentrop, and E. van der Heide. "Leading edge erosion of coated wind turbine blades: Review of coating life models". In: *Renewable Energy* 80 (2015), pp. 837–848.

[44] B. Fitzsimons and T. Parry. "Coating Failures and Defects". In: 2016.

[45] J.A. Sainz. "New Wind Turbine Manufacturing Techniques". In: *Procedia Engineering* 132 (2015). MESIC Manufacturing Engineering Society International Conference 2015., pp. 880–886. ISSN: 1877-7058. URL: http://www.sciencedirect.com/science/article/pii/S1877705815044859.

[46] D. Eisenberg, S. Laustsen, and J. Stege. "Wind turbine blade coating leading edge rain erosion model: Development and validation". In: *Wind Energy* 21.10 (2018), pp. 942–951. URL: https://onlinelibrary.wiley.com/doi/abs/10.1002/we.2200.

[47] P. Greaves. "6 - Design of offshore wind turbine blades". In: *Offshore Wind Farms*. Ed. by Chong Ng and Li Ran. Woodhead Publishing, 2016, pp. 105–135. ISBN: 978-0-08-100779-2. URL: http://www.sciencedirect.com/science/article/pii/B9780081007792000064.

[48] D. Seghier. *Erosion Sensors for continuous monitoring of coatings (EROSCANS)*. 2017. URL: https://gtr.ukri.org/projects?ref=132871.

[49] 3M. URL: https://multimedia.3m.com/mws/media/1226740O/3m-wind-products-catalog-rev-b.pdf.

[50] M. Froese. "Maximizing wind-farm ROI through blade protection and repair". In: (2015). URL: https://www.windpowerengineering.com/maximizing-wind-farm-roi-through-blade-protection-and-repair/.

[51] 3M. 2017. URL: https://multimedia.3m.com/mws/media/1277254O/3m-wind-protection-tape-2-0-application-guide.pdf.

[52] Philippe Giguère and Michael Selig. "Aerodynamic effects of leading-edge tape on airfoils at low Reynolds numbers". In: *Wind Energy* 2 (1999), pp. 125–136. DOI: 10.1002/(SICI)1099-1824(199907/09)2:33.0.CO;2-5.

[53] Olivier Cleynen. *Wing profile nomenclature*. 2011. URL: https://en.wikipedia.org/wiki/File:Wing_profile_nomenclature.svg.

[54] S. Chinmay. "Turbine blade erosion and the use of wind protection tape". University of Illinois at Urbana-Champaign, 2012.

[55] N. Kidder. "Aerodynamic Impact of Leading Edge Surface Treatments on Wind Turbine Blades". The Ohio State University, 2015.

[56] *AmourEDGE Website - A new leading edge protection for wind turbine blades*. URL: https://www.armouredge.com.

[57] W.D. Weigel. *Advanced rotor blade erosion protection system*. 1996. URL: https://apps.dtic.mil/sti/pdfs/ADA314355.pdf.

[58] W.A. Thomas, C. Yu, S.C. Hong, and E.L. Rosenzweig. "Enhanced erosion protection for rotor blades". In: *American helicopter safety 65th annual forum* (2009).

[59] *Fundamentals of adhesive bonding of composite materials*. 2017.

[60] K.C. Shin and J.J. Lee. "Tensile load-bearing capacity of co-cured double lap joints". In: (2003). DOI: https://doi.org/10.1163/156856100742366.

[61] H.T.X. Truong. "An experimental and computational study on Co-cured metal-polymer matrix composite interfaces in high temperature hybrid laminates". PhD thesis. 2016.

[62] S. Masson. "Numerical investigation of droplet trajectories in a raindrop erosion test bench". 2019.

[63] Samir Chandra Roy, Jean-Pierre Franc, Christian Pellone, and Marc Fivel. “Determination of cavitation load spectra – Part 1: Static finite element approach”. In: *Wear* (2015).

[64] Samir Chandra Roy, Jean-Pierre Franc, Nicolas Ranc, and Marc Fivel. “Determination of cavitation load spectra – Part 2: Dynamic finite element approach”. In: *Wear* (2015).

[65] Marc Fivel, Jean-Pierre Franc, and Samir Chandra Roy. “Towards numerical prediction of cavitation erosion”. In: *Interface Focus* (2015).

[66] “Primer on the simplest inelastic model: non-Hardening von Mises (J2) plasticity”. In: (). URL: https://csm.mech.utah.edu/content/wp-content/uploads/2011/10/9tutorialOnJ2Plasticity.pdf.

[67] *von Mises yield criterion*. URL: https://en.wikipedia.org/wiki/Von_Mises_yield_criterion?oldformat=true.

[68] “Mechanical Behavior, Testing and Manufacturing Poperties of Materials”. In: (2009).

[69] NITIN P. WASEKAR, PRATHAP HARIDOSS, and G. SUNDARARAJAN. “Solid Particle Erosion of Nanocrystalline Nickel Coatings: Influence of Grain Size and Adiabatic Shear Bands”. In: *The Minerals, Metals Materials Society and ASM International* (2017).

[70] R. Rajendran, M. Venkateshwarlu, V. Petley, and S. Verma. “Strain hardening exponents and strength coefficients for aeroengine isotropic metallic materials - a reverse engineering approach”. In: *Journal of the Mechanical Behavior of Materials* (2014).

[71] C. Fallon and G.J. McShane. “Fluid-structure interactions for the air blast loading of elastomer-coated concrete”. In: *International Journal of Solids and Structures* (2019), pp. 138–152.

[72] T.K. Mauchien. “A fracture mechanics approach to accelerated life testing for cathodic delamination at polymer/metal interface”. In: (2013).

[73] Gong-Dong Wang and Stephen Kirwa Melly. “Three-dimensional finite element modeling of drillingCFRP composites using Abaqus/CAE: a review”. In: *Int J Adv Manuf Technol* (2018).

[74] *Abaqus Documentation*. URL: https://abaqus-docs.mit.edu/2017/English/SIMACAEEXCRefMap/simaexc-c-docproc.htm.

[75] S. Abedini, C. Dong, and I.J. Davies. “Multi-objective particle swarm optimisation of multilayer functionally graded coating systems for improved interfacial delamination resistance”. In: *Materials Today Communication* 24 (2020). DOI: https://doi.org/10.1016/j.mtcomm.2020.101202.

UNIVERSITÉ CATHOLIQUE DE LOUVAIN
École polytechnique de Louvain
Rue Archimède, 1 bte L6.11.01, 1348 Louvain-la-Neuve, Belgique | **www.uclouvain.be/epl**